INFORMATION TO USERS

This material was produced from a microfilm copy of the original document. While the most advanced technological means to photograph and reproduce this document have been used, the quality is heavily dependent upon the quality of the original submitted.

The following explanation of techniques is provided to help you understand markings or patterns which may appear on this reproduction.

1. The sign or "target" for pages apparently lacking from the document photographed is "Missing Page(s)". If it was possible to obtain the missing page(s) or section, they are spliced into the film along with adjacent pages. This may have necessitated cutting thru an image and duplicating adjacent pages to insure you complete continuity.

2. When an image on the film is obliterated with a large round black mark, it is an indication that the photographer suspected that the copy may have moved during exposure and thus cause a blurred image. You will find a good image of the page in the adjacent frame.

3. When a map, drawing or chart, etc., was part of the material being photographed the photographer followed a definite method in "sectioning" the material. It is customary to begin photoing at the upper left hand corner of a large sheet and to continue photoing from left to right in equal sections with a small overlap. If necessary, sectioning is continued again — beginning below the first row and continuing on until complete.

4. The majority of users indicate that the textual content is of greatest value, however, a somewhat higher quality reproduction could be made from "photographs" if essential to the understanding of the dissertation. Silver prints of "photographs" may be ordered at additional charge by writing the Order Department, giving the catalog number, title, author and specific pages you wish reproduced.

5. PLEASE NOTE: Some pages may have indistinct print. Filmed as received.

University Microfilms International
300 North Zeeb Road
Ann Arbor, Michigan 48106 USA
St. John's Road, Tyler's Green
High Wycombe, Bucks, England HP10 8HR

Downloaded from SHAREOK. Persistent Handle URL: https://hdl.handle.net/11244/4224

77-12,734

CHAPLIN, Wallace Herman, Jr., 1943-
RADIATION BUDGETS OF THE TROPOSPHERE OVER THE EAST CHINA SEA DURING THE AIR-MASS TRANSFORMATION EXPERIMENT (AMTEX) 1974.

The University of Oklahoma, Ph.D., 1976
Physics, atmospheric science

Xerox University Microfilms, Ann Arbor, Michigan 48106

© 1977

WALLACE HERMAN CHAPLIN, JR.

ALL RIGHTS RESERVED

THE UNIVERSITY OF OKLAHOMA

GRADUATE COLLEGE

RADIATION BUDGETS OF THE TROPOSPHERE OVER THE EAST CHINA SEA DURING THE AIR-MASS TRANSFORMATION EXPERIMENT (AMTEX) 1974

A DISSERTATION

SUBMITTED TO THE GRADUATE FACULTY

in partial fulfillment of the requirements for the

degree of

DOCTOR OF PHILOSOPHY

BY

WALLACE H. CHAPLIN, JR.

Norman, Oklahoma

1976

RADIATION BUDGETS OF THE TROPOSPHERE OVER THE EAST CHINA SEA DURING THE AIR-MASS TRANSFORMATION EXPERIMENT (AMTEX) 1974

APPROVED BY

James F Kimpel

M. Rasmussen

Claude E Duchon

Eugene M Wilkins

Jay S. Fein

DISSERTATION COMMITTEE

ACKNOWLEDGMENTS

The author wishes to express his gratitude to the United States Air Force, the Air Force Institute of Technology for the opportunity to carry out this graduate study. Thanks are due the USAF Environmental Technical Applications Center, a part of Air Weather Service, for providing the Air Force Global Weather Central Three Dimensional Nephanalyses used in this research.

Very sincere appreciation is given to Dr. James F. Kimpel, whose encouragement, suggestions, assistance and guidance were essential to this work. The review and helpful criticism of this manuscript by Dr. Claude E. Duchon, Dr. Jay S. Fein, Dr. Maurice L. Rasmussen, and Dr. Eugene M. Wilkins is also appreciated. Thanks also go to Dr. Mads Ledet who served on my advisory committee during early portions of my graduate program.

I am also grateful to my fellow graduate students, particularly Captain Peter Soliz, Pamela Stevens, and Steven Amburn, for the help they provided during my research. The assistance of Jo Ann Oberst and Joan Kimpel in the preparation of this manuscript is also appreciated.

I am especially thankful to my wife, Pat, and children, Marcia, Brenda, Kim and Eric who patiently and understandingly

shared me with this work.

This dissertation was accomplished in connection with graduate study at the University of Oklahoma and was sponsored in part by the Atmospheric Sciences Section, National Science Foundation under grant ATM74-23024.

ABSTRACT

Radiative budgets of the troposphere are highly dependent upon cloud conditions present. Thus, estimates of quantities for these budgets taken from climatological studies are not applicable to specific cases of cyclone development and/or strong air mass modification situations of particular interest to the Air Mass Transformation Experiment (AMTEX).

A radiation scheme, using cloud information obtained from the operational Three Dimensional Nephanalysis (3DNEPH) Model of the Air Force Global Weather Central (AFGWC), was developed to study radiative transfer during different synoptic conditions during AMTEX '74. Improvements have been made to an older technique to include more adequate treatment of stratospheric radiative transfer by water vapor, carbon dioxide and ozone; better treatment of Rayleigh scattering; multiple reflections of radiation between cloud layers; and incorporation of temperature dependent long wave emissivities.

Calculations are performed at a grid spacing of approximately 196 km using composite 3DNEPH analyses and AMTEX six-hourly upper-air, surface, and ship observations. Vertical resolution of the model is 50 mb.

Comparisons of calculated irradiance components with

measured values support the contention that the model provides acceptable results when the cloud data, which are spacial estimates, are representative of the location where the model is applied. At particular points (stations) and times where the cloud layers used in the model appeared representative of the clouds reported on the surface observation, the downward fluxes of short wave and long wave radiation estimated as reaching the surface were within 9.0 percent and 3.8 percent of the respective flux measurements.

Three synoptically significant days are examined: 18 February (warm day), 23 February (FROPA day), and 26 February (cold day), 1974. Significant variations in tropospheric budgets and radiational cooling rates result from day to day, and grid point to grid point, primarily due to varying cloudiness conditions. Net tropospheric cooling rates of 0.941 $^{\circ}C\ day^{-1}$, 0.981 $^{\circ}C\ day^{-1}$ and 0.711 $^{\circ}C\ day^{-1}$ are obtained over the region for the respective three days. These radiative cooling rates are within 4.5 percent, 9.0 percent and 21.0 percent, respectively of a climatological net cooling rate obtained in another study for the latitude area and season of AMTEX. Values of 0.36, 0.56, and 0.59 are estimated for the effective albedo at 100 mb on these days.

The fact that the average net radiative loss by the atmospheric column was larger during the warm day than the cold day suggests that the net radiative contribution to air mass modification is a reduction in cooling, or possibly even warming

over the region.

The model developed in this research does not lend itself to real time operational use at present because of the time and computer storage required to carry out the calculations. Continued effort should be made not only to improve the radiative techniques used in the model, but also to develop increasingly efficient algorithms.

TABLE OF CONTENTS

		Page
ACKNOWLEDGMENTS		iii
ABSTRACT		v
LIST OF TABLES		ix
LIST OF FIGURES		xi
Chapter		
I.	INTRODUCTION	1
II.	DATA	6
III.	GRID CONSTRUCTION AND DATA OBJECTIVE ANALYSIS	8
IV.	METHODOLOGY	11
	A. Infrared Radiation - Clear Sky	12
	B. Infrared Radiation - Cloudy Sky	16
	C. Solar Radiation Components	17
	D. Solar Radiation - Clear Sky	18
	E. Solar Radiation - Cloudy Sky	21
	F. Net Radiational Cooling	25
	G. Surface Radiation Budget	26
V.	RESULTS	28
	A. Synoptic Situation During AMTEX '74	28
	B. Time and Spacial Variations of Clouds Over the AMTEX '74 Region	29
	C. Comparison of Observed and Calculated Radiation Components	31
	D. Effects of Clouds on Tropospheric Radiation Budgets	34
	E. Time and Spacial Variations of Atmospheric Radiation Over the AMTEX '74 Region	36
VI.	SUMMARY AND RECOMMENDATIONS	42
BIBLIOGRAPHY		47
APPENDIX A.	Cloud Analysis Model	53

LIST OF TABLES

Table		Page
1.	List of Japan Meteorological Agency stations used in this study.	60
2.	Stratospheric vertical distribution of ozone and temperature used in radiation flux calculations.	61
3.	Carbon dioxide flux emissivity as a function of optical depth, u, and temperature.	62
4.	Water vapor flux emissivity as a function of optical depth, u, and temperature	63
5.	Ozone flux emissivity as a function of optical depth, u, and temperature	64
6.	Flux emissivity correction quantity for water vapor-carbon dioxide overlap at -70 C	65
7.	Flux emissivity correction quantity for water vapor-carbon dioxide overlap at -40 C	66
8.	Flux emissivity correction quantity for water vapor-carbon dioxide overlap at -10 C	67
9.	Flux emissivity correction quantity for water vapor-carbon dioxide overlap at 20 C.	68
10.	Empirical constants used in Eqs. (15) and (16). . .	69
11.	The function $\eta(\varphi)$ used in Eq. (17) for calculating absorption by the 9.6 μ band of ozone	70
12.	Transmission, T, reflection, R, and absorption, A, values for low clouds as a function of solar zenith angle, ψ, used for the I_a^o component of the solar radiation	71
13.	Transmission, T, reflection, R, and absorption, A, values for middle clouds as a function of solar zenith angle, ψ, used for the I_a^o component of the solar radiation.	72
14.	Transmission, T, reflection, R, and absorption, A, values for high clouds as a function of solar zenith angle, ψ, used for the I_a^o component of the solar radiation	73

Table		Page
15.	Significant weather events during AMTEX '74	74
16.	Spacially averaged cloud estimates for the AMTEX region on 18, 23 and 26 February 1974	75
17.	Clear sky and cloud contributions to the radiative budget components at Naha on February 23, 1974, 0900 JST.	76
18.	The long wave and short wave radiation budgets of the troposphere for February 18, 23, and 26, 1974 .	77
A1.	Bases and tops of the 15 layers of the 3DNEPH cloud analysis.	78

LIST OF FIGURES

Figure		Page
1.	Geographic region around the Southwest Islands of Japan and station locations during AMTEX. . . .	79
2.	Station locations during AMTEX, and grid squares for which cloud information from the 3DNEPH is available. Circled grid points represent the 6 by 6 grid field established for this study	80
3.	Response function for the exponential weighting function for varying values of k	81
4.	Schematic representation of the radiation budgets of the atmospheric column from 100 mb to the surface	82
5.	The 6 by 6 grid field established for this study .	83
6.	Mean daily total cloud cover at the grid points used for this study.	84
7.	Mean daily low cloud cover at the grid points used for this study.	85
8.	Mean daily middle cloud cover at the grid points used for this study.	86
9.	Mean daily high cloud cover at the grid points used for this study.	87
10.	Percent difference for the calculated long wave, short wave and total downward fluxes at the surface on February 18, 23 and 26, 1974, at the stations for which measurements were made.	88
11.	Vertical profiles of terrestrial cooling, solar heating, and net radiational cooling for a grid point in AMTEX on February 23, 1974.	89
12.	Downward long wave fluxes at 100 mb at the grid points used for this study	90
13.	Upward long wave fluxes at 100 mb at the grid points used for this study	91

Figure		Page
14.	Net long wave fluxes at 100 mb at the grid points used for this study	92
15.	Downward long wave fluxes at the surface at the grid points used for this study.	93
16.	Upward long wave fluxes at the surface at the grid points used for this study.	94
17.	Net long wave fluxes at the surface at the grid points used for this study	95
18.	The amount of short wave radiation subject to absorption that is input at 100 mb at the grid points used for this study	96
19.	The amount of the short wave radiation component subject to absorption that is reflected upward by the clouds at the grid points used for this study.	97
20.	The amount of the short wave radiation component subject to absorption that reaches the surface through clouds at the grid points used for this study.	98
21.	The amount of the short wave radiation component subject to absorption that reaches the surface through clear sky at the grid points used for this study	99
22.	The amount of short wave radiation subject to scattering that is input at 100 mb at the grid points used for this study	100
23.	The amount of the short wave radiation component subject to scattering that is scattered upward by the clouds and atmosphere at the grid points used for this study.	101
24.	The amount of the short wave radiation component subject to scattering that reaches the surface through clouds at the grid points used for this study.	102
25.	The amount of the short wave radiation component subject to scattering that reaches the surface through clear sky at the grid points used for this study	103

Figure		Page
26.	The sum of the amounts of short wave radiation components subject to absorption and scattering that reaches the surface and is reflected at the grid points used for this study.	104
27.	Net upward irradiance (long and short wave) at 100 mb at the grid points used for this study. . .	105
28.	Net downward irradiance (long and short wave) at the surface at the grid points used for this study.	106
29.	Absorption of long wave radiation at the grid points used for this study	107
30.	Absorption of short wave radiation at the grid points used for this study	108
31.	Long wave radiational cooling rate from 100 mb to the surface at the grid points used for this study.	109
32.	Short wave radiational heating rate from 100 mb to the surface at the grid points used for this study.	110
33.	Net radiational cooling rate from 100 mb to the surface at the grid points used for this study . .	111
34.	Schematic representation of the average radiation budgets of the atmospheric column from 100 mb to the surface for February 18, 23 and 26, 1974, in the AMTEX area	112
A1.	Example of the type of information available for the composite three layer cloud analysis derived from the 3DNEPH data	113
A2.	Schematic diagram of the eight possible situations a stream of radiation could encounter with three cloud layers present.	114

RADIATION BUDGETS OF THE TROPOSPHERE OVER THE EAST CHINA SEA DURING THE AIR-MASS TRANSFORMATION EXPERIMENT (AMTEX) 1974

CHAPTER I

INTRODUCTION

Radiative processes in the atmosphere and at the earth's surface strongly influence the origin of atmospheric motions and are vital for their maintenance. In the mean, the earth's surface receives more radiative energy from the sun than it loses in the form of terrestrial radiation; the earth's surface experiences a net radiation gain, while the atmosphere experiences a net loss. This radiation imbalance requires a transfer of energy from the surface to the atmosphere. This can be in the form of the transfer of sensible and latent heat, the origin of thermal turbulence, and the formation of convection. The non-uniformity of solar radiation income at different latitudes leads to a considerable horizontal temperature gradient in the troposphere. As a consequence, the atmosphere must compensate for the non-uniformity in the distribution of heat by transferring the heat poleward from low to high latitudes. In addition, the horizontal differences in the radiation

budgets between low and high latitudes build baroclinic patterns in which the dynamic systems develop and by which they are modified. On the other hand, the dynamic systems, especially through water vapor and cloud distributions, modify the radiation fields. It is therefore essential that forecast and general circulation models take radiative processes into account.

Early knowledge of the radiative balance of the atmosphere was based on contributions of Simpson (1928), and Baur and Phillips (1934, 1935). Simpson recognized the importance of the spectral distribution of water vapor absorption. He used a simple model to calculate the distribution of incoming and outgoing radiation as a function of latitude and season. Baur and Phillips improved on Simpson's work by integrating the equations of radiative transfer in the atmosphere for cases of a more reasonable atmospheric model. During the same period, Mügge and Möller (1932) devised a graphical method for calculating radiative flux in the atmosphere. The results were in the form of a radiation chart. Möller (1935) later used this chart to present the first reasonably complete picture of the vertical structure of the heat balance within the mid-latitude troposphere.

With further resolution of the infrared spectrum of water vapor and new observations and calculations of the average albedo of clouds, reevaluations of the atmospheric radiation budget were carried out in the late 1930's and early 1940's. New values for infrared transmission in the atmosphere, based

on the spectral line shape and a considerably improved knowledge of the infrared absorption spectrum of the major atmospheric absorbents, were derived by Elsasser (1938) and Schmidt (1939). This was followed by two improved atmospheric radiation charts (Elsasser, 1942; and Möller, 1943). Additional calculations of the water vapor spectrum resulted in other charts (Robinson, 1950; and Yamamoto, 1952).

Yamamoto (1953), Houghton (1954), London (1957), Manabe and Möller (1961), and Davis (1963), among others, have theoretically approached the problem concerning the distribution of the radiation budget in the earth - atmosphere system. However, most of them only calculated meridional distributions and seasonal variations. Katayama (1966 and 1967a, b) undertook calculations of the geographical distribution of the mean radiation budget of the earth and atmosphere based on more extensive climatic data than had been available before. Dopplick (1972) obtained monthly zonal global radiative heating rates from the surface to 10 mb for all twelve months. However, results from these previous studies and the research of others (e.g. Budyko, 1963; Rodgers, 1967; and Kondratyev, 1972) cannot be strictly applied to shorter term calculations involving a particular geographic area.

A scientific program called the Air Mass Transformation Experiment (AMTEX) was carried out over the Southwest Islands of Japan during February 1974 and February 1975. The aim of AMTEX is to clarify the transfer processes by which energy and

momentum are supplied from the sea surface to the air and transported to the free atmosphere during rapid modification of an air mass as it moves from one region to another region with a very different characteristic lower boundary. Such a phenomenon occurs when cold dry continental air sweeps off the east coast of Asia over warm water in the vicinity of the Southwest Islands of Japan. The geographic region around these islands is shown in Figure 1. This experiment on air-sea interaction developed by the Japanese National Committee for GARP (Global Atmospheric Research Program) affords an opportunity to examine the spatial and daily variations of atmospheric radiation over a particular region.

Kimpel (1973) examined the net radiational heating of the tropical atmosphere - ocean system and the subsequent export of energy poleward in the Marshall Islands region. The present research takes an approach similar to that of Kimpel in calculating the radiation budgets of the troposphere over the East China Sea during AMTEX.

The purpose of this study is to (1) develop a model that will provide realistic values for radiative transfer in a cloudy atmosphere; (2) improve on Kimpel's technique to include the use of the US Air Force Global Weather Central, three dimensional nephanalysis (3DNEPH) data (Coburn, 1971) in a unique estimate of radiative transfer, provide better treatment of Rayleigh scattering by air molecules and water vapor, include multiple reflections of radiation between cloud layers, and

treat more adequately stratospheric radiative transfer by water vapor, carbon dioxide and ozone; (3) to compare calculated irradiance components with measured values to test the accuracy of the model. The results of this research should be helpful in constructing an overall energy budget for the AMTEX region, and can also help in future studies of radiation budgets, baroclinic instability, and radiative contributions to such things as convection, thickness tendency and vorticity.

CHAPTER II

DATA

Surface and radiosonde data collected in the East China Sea during AMTEX 1974 are used in this study. Stations where the data have been collected are shown in Figure 2 and Table 1. Upper air soundings of pressure, temperature, and humidity were made four times daily at the locations shown. Surface synoptic data obtained hourly at Naha, Minamidaitojima, Ishigakijima, Miyakojima, and Naze are used, as are incoming short wave and downward total radiation flux measurements at the land stations: Naze, Naha, Mijakojima and Minamidaitojima, and the three ship stations: Ryofu-maru, Keifu-maru, and Nojima.

Continuous records of the radiation components have been obtained to the nearest thousandth of a langley per minute. The surface pressures are given to the nearest tenth of a millibar, the constant pressure levels to the nearest geopotential meter, temperatures to the nearest tenth of a degree centigrade, and humidity to the nearest whole percent.

Magnetic tapes of cloud data from the 3DNEPH program have been obtained from the U.S. Air Force Environmental Technical Applications Center, Washington, DC, and are included in the radiation calculations.

The 3DNEPH model, and modifications made to the data for this study are described in Appendix A. The grid squares for 3DNEPH cloud data are shown in Figure 2.

Sea surface temperature data were received from the three research ships listed in Table 1, the research ship Chofu Maru which moved around the entire AMTEX area, and from seventy-one cooperative transient ships. Of these, only twenty-six passed through or close enough to the area to make their data useful. Amburn (1976) objectively analyzed the sea surface temperatures and provided his analyses for this study.

CHAPTER III

GRID CONSTRUCTION AND DATA OBJECTIVE ANALYSIS

The surface and upper-air data analyses were made on a 6 by 6 grid field established on a polar stereographic map projection true at 60 degrees north latitude and centered at 170 degrees east. The distance between grid points is 190.5 kilometers or one-half inch on the map. This size grid was chosen due to the amount of time required for the radiation calculations and somewhat limited computer resources. This grid, a subset of the grid over which 3D NEPH data is available, is depicted in Figure 2.

In order to carry out the radiation calculations in the troposphere, fields of pressure, humidity and temperature at the surface, and humidity and temperature at nineteen levels, in 50 mb increments, from 1000 mb to 100 mb were specified through objective analysis of the surface and upper air observations of the eight stations listed in Table 1. The objective analysis assigns values of the parameters to the regularly spaced grid points from the irregularly spaced observation points.

The analysis used in this study assigns a grid point value as the weighted average of the surrounding observations by using

the expression

$$\Phi_{ij} = \frac{\Sigma W_m \Phi_m}{\Sigma W_m} , \qquad (1)$$

where Φ_m and Φ_{ij} are the variable values at the observation point and grid point respectively, and W_m is the weight for that observation point. Each observation is weighted according to a prespecified relationship and the sum of these weighted observations is normalized by the sum of the weights.

Horizontal wind components and variables advected by the wind are anisotropic and non-homogeneous (Gandin, 1965). Sasaki (1971) has provided a theoretical basis for the use of anisotropic weight functions through numerical variational analysis; and McFarland (1975) has shown that, when an isotropic, homogeneous weight function is used for objective analysis of anisotropic, non-homogeneous variables, errors may be introduced in the computations. These facts are recognized. However, because wind information was not available at the research vessels Ryofu Maru and Nojima, nor at all nineteen levels of this study for the other stations, the weight function used in the present research is Barnes (1973) exponential weight function. This isotropic, homogeneous weight function is defined as

$$W = \exp \left\{ \frac{-(x^2 + y^2)}{4k} \right\} , \qquad (2)$$

where $x^2 + y^2$ is the distance squared from the observation point to the grid point, and k is an arbitrary smoothing parameter.

Choice of the parameter k, in the application of Eq. (2),

is based on the minimum resolvable wavelength of the grid. This minimum resolvable wavelength can be found in the following manner. For each station, the distance to the closest station is calculated. These distances are summed and divided by the total number of stations to get the average distance Δx. Analytically, two points separated by Δx are insufficient to determine a wavelength. Three points, hence 2 Δx, are required to define the minimum resolvable wavelength.

This weight function, Eq. (2), has several desirable features cited by Barnes. First because the weight function approaches zero asymptotically, the influence of data can be extended any distance without changing the weight function. This is very desirable for two reasons. At times it is convenient to cut off computations of weights beyond a certain radius where the influence is minimal, thereby saving computation time. Also, in data sparse areas, the scanning radius may be extended. Another feature is that the fields may be smoothed to any desired degree through the parameter k.

Barnes has shown the response function of Eq. (2) to be

$$r_f = \exp\ (-k\ \pi^2/\lambda^2)\ , \qquad (3)$$

where λ is wavelength. Fig. 3 shows the response function for different values of k. For this study the parameter k was chosen to be 7 to provide a weight function, W, of 0.1 at 4 grid intervals.

CHAPTER IV

METHODOLOGY

The radiative budget of the troposphere depends on the distribution of incoming solar radiation and outgoing solar and terrestrial radiation. For the distribution of incoming radiation, one must consider: a) the energy received at the top of the atmosphere; b) the depletion of this energy as the solar beam penetrates the atmosphere; c) the reflection of the solar beam by clouds, atmosphere and earth's surface; and d) the scattering of the solar beam. The outgoing terrestrial radiation is a function of the temperature at the surface and in the atmosphere, and the cloudiness and distribution of atmospheric aerosols and constituents such as water vapor, carbon dioxide, and ozone.

There is also a dependence on time and geometry through the variation of sun angle. Thus, in order to obtain theoretically consistent results, it is necessary to depict the atmosphere by a realistic physical model.

The methods used in this research for the estimation of the radiative budget of the troposphere are covered in the following sections. Included are discussions of calculating

infrared radiation fluxes under clear and cloudy sky conditions, partitioning solar radiation components, estimating solar radiation fluxes in clear and cloudy skies, obtaining net radiational cooling rates throughout the troposphere, and arriving at surface radiation budgets. The basic equations for calculating fluxes are stated. Derivations of these equations can be found in Goody (1964).

A. Infrared Radiation - Clear Sky

Flux or slab emissivity, ε_f, of each gaseous absorber is defined as the ratio of infrared flux to black body flux at the same temperature T, and is given by

$$\varepsilon_f(u,T) = \frac{F(u,T)}{F_b} , \tag{3}$$

where u is the optical depth (thickness) of the absorber. F_b, the black body flux in Eq. (3), may be replaced by σT^4 giving the expression,

$$\varepsilon_f(u,T) = \frac{F(u,T)}{\sigma T^4} , \tag{4}$$

where σ is the Stefan-Boltzman constant ($.817 \times 10^{-10}$ ly min^{-1} $^oK^{-4}$).

The optical depth, u_{H_2O}, for water vapor is expressed as the total length of liquid which may be precipitated out of the path per unit area. The unit used is precipitable centimeters (pr cm). This optical depth is computed from the mixing ratio distribution via the hydrostatic equation, assuming that the mixing ratio of water vapor within the slab is constant at

a value given by the arithmetic mean of mixing ratios at its bounding surfaces. This increment of optical depth, du, is then $\bar{q} \frac{dp}{g}$, where $\bar{q}$ is mean mixing ratio, p is pressure, and g is acceleration due to gravity. The mixing ratio of stratospheric water vapor is taken as 0.002 g K_g^{-1}, and values are interpolated between the stratosphere and the upper-most level for which radiosonde humidity measurements are available.

The optical depths, u_{CO_2} and u_{O_3}, for carbon dioxide and ozone respectively are expressed in units of atmospheric centimeters (atm cm). One atmospheric centimeter is equivalent to a length of 1 cm of gas at standard temperature (0°C) and pressure (1013.25 mb).

The optical depth, u_{CO_2} in atmospheric centimeters, for carbon dioxide is estimated in the following manner. It is assumed that carbon dioxide in the atmosphere is uniformly mixed and therefore constant in space and time. Taking the amount of carbon dioxide as 0.032 percent by volume, the effective amount of carbon dioxide between any two pressure levels is then 0.260 atm cm mb^{-1} (McClatchey, et al., 1972).

The total optical mass of ozone at 50 mb and above is taken as 0.212 atm cm (Craig, 1965). The vertical distribution of the optical depth, u_{O_3} in atmospheric centimeters, for ozone is given in Table 2. Also shown in that table is the temperature profile for the stratosphere used in obtaining the downward radiance at 100 mb. The temperatures are those of the U.S. Standard Atmosphere 1962, (COESA, 1962).

The water vapor, carbon dioxide, and ozone optical depths must be adjusted due to pressure broadening, the process in which the width of the "lines" in an emission spectrum or absorption spectrum of a gaseous radiative medium is increased due to perturbations of the energy states by collisions of the molecules or atoms within the gas. Although the effect of pressure broadening is very small at atmospheric temperatures, it plays an important role in the radiative balance of the troposphere. A complete discussion of pressure broadening can be found in Goody (1964) and Kondratyev (1969).

Infrared emission from the "wings" of water vapor lines that are pressure broadened in the lower troposphere is of a wavelength that is not strongly absorbed in the lower-pressure region of the upper troposphere. The resultant escape of radiation from the wings is an important part of the net upward flux of long-wave radiation in the troposphere. As a result, a "corrected" optical depth for water vapor,

$$u^* = u \left(\frac{\bar{p}}{p_o}\right)^{\gamma} \left(\frac{T_o}{\bar{T}}\right)^{0.5} , \qquad (5)$$

must be used, where γ is an empirically derived constant. Kuhn (1962, 1963) found evidence that a single pressure-reduced water vapor optical depth will not serve over a wide range of optical depths. He implies a non-linear pressure reduction to optical depth of water vapor leading to a $\gamma(p)$ relationship of the form,

$$\gamma(p) = (0.1221 + 0.00177\bar{p} - 0.00000105\bar{p}^2) , \qquad (6)$$

which is used for water vapor in this research, where $\bar{p}$ is expressed in millibars.

For a pressure reduction to carbon dioxide optical depths, the pressure scaling is of the form $(\frac{\bar{P}}{P_o})^{0.5}$ and temperature scaling of the form $(\frac{T_o}{\bar{T}})^{0.6}$. For ozone, the pressure scaling is of the form $(\frac{\bar{P}}{P_o})$ and temperature scaling of the form $(\frac{T_o}{\bar{T}})^{0.5}$. In the following discussions, the optical depths have been corrected, and u is taken to mean u*.

The flux arising from the infrared emission and transmission in an isothermal atmosphere above or below any level follows from Eq. (4) and is given by

$$F(u,\bar{T}) = \epsilon_f(u,\bar{T})\ \sigma\ \bar{T}^4 \ . \tag{7}$$

To obtain the flux as a function of optical depth for an atmospheric slab, Eq. (7) is differentiated with respect to u, giving

$$\frac{dF(u,\bar{T})}{du} = \sigma\ \bar{T}^4\ \frac{d\epsilon_f(u,\bar{T})}{du} \ . \tag{8}$$

Considering an atmosphere with arbitrary vertical distribution of radiating materials, and assuming horizontal stratification, that is u, T, and T_d are functions of height alone; Eq. (8), integrated over thin layers of optical depth, each with an assumed constant temperature, $\bar{T}$, gives

$$F_r(u,\bar{T})\downarrow = \int_o^u \sigma\ \bar{T}^4\ \frac{\partial \epsilon_f(u,\bar{T})}{\partial u}\ du \ , \tag{9}$$

for the downward flux at a reference level, r. The integration is carried out from the top of the atmosphere downward to the reference level.

The upward flux, $F_r(u,\bar{T})\uparrow$, is given similarly except a term for the transmitted surface radiation must be added. Flux transmissivity, assuming no reflections, is defined as

$$\tau_f(u,\bar{T}) = 1.0 - \epsilon_f(u,\bar{T}) \quad . \tag{10}$$

Therefore Eq. (8), including the transmitted surface radiation, may be integrated over thin layers of optical depths giving

$$F_r(u,\bar{T})\uparrow = \int_o^u \sigma \bar{T}^4 \frac{\partial \epsilon_f(u,\bar{T})}{du}\, du + (1.0 - \int_o^u \frac{\partial \epsilon_f(u,\bar{T})}{du}\, du)\, \sigma T_o^4 \quad , \tag{11}$$

for the upward flux, where T_o is the surface temperature. The integration is carried out from the reference level downward to the air-surface interface.

Values of flux emissivity, as a function of temperature, versus optical depth of carbon dioxide, water vapor and ozone after Staley and Jurica (1970), are used in the calculation of infrared fluxes. They are given in Tables 3, 4, and 5. The small contribution due to ozone and other minor constituents is ignored in the troposphere. In order to account for overlap in the rotation bands of water vapor and carbon dioxide, a correction must be applied. The correction, as a function of temperature is given in Tables 6-9 (Staley and Jurica, 1970).

B. Infrared Radiation - Cloudy Sky

Clouds are important absorbers and emitters of infrared radiation. They are treated as a black body. The temperatures of cloud bases and tops are taken from radiosonde data at the

corresponding levels. Thus, all longwave radiation arriving at a horizontal surface is absorbed and all outgoing radiation is considered black. In this manner, both the upward and downward radiative components are obtained at the cloud bases and tops. The upward and downward fluxes in the clear sky regions between the ocean surface, clouds, and upper reference level are computed using the clear sky technique described previously.

C. Solar Radiation Components

The solar radiation will be divided into two components: the part subject to scattering and the part subject to absorption (Joseph, 1970). Thus, the short wave radiation incident at the top of the atmosphere, I_o, at zenith angle, ψ, is separated as follows:

The part subject to scattering: $I_o^s = 0.651\ I_o \cos\psi$ (12)

The part subject to absorption: $I_o^a = 0.349\ I_o \cos\psi$. (13)

The first component of the short wave radiation (Eq. 12), I_o^s, is subject to Rayleigh scattering but not to absorption. It contributes only to earth-surface insolation, after scattering and reflective attenuations (by clouds) in the column above the earth are considered. The scattering is assumed to be nearly isotropic; that is, half of the scattered radiation is sent backward and the other half is sent forward (Humphreys, 1940 and Tousey, et al., 1947). This is a valid assumption since the diameters of molecular particles of dry air (mainly nitrogen and oxygen) and water vapor are considerably smaller

than the wave lengths of solar radiation. Secondary scattering in the atmosphere is not taken into account. That is, it is assumed that the scattered radiation will continue to travel upwards and downwards as diffuse radiation without any further scattering.

The second component of the short wave radiation (Eq. 13), I_o^a, is subject to water vapor, carbon dioxide and ozone absorption, but not to Rayleigh scattering, and contributes to atmospheric heating.

D. Solar Radiation - Clear Sky

The total solar flux, F, absorbed above a pressure level, p, summed over all spectral bands, i, is written as

$$F = \sum_i I_{o_i}^a \cos\psi A_i \ . \qquad (14)$$

$I_{o_i}^a$ is the mean solar intensity of the ith band in erg cm^{-2} sec^{-1} (wave number)$^{-1}$ taken from Allen (1958); $\sum_i$ denotes summation over all relevant water vapor and carbon dioxide bands; and A_i denotes absorption in cm^{-1} of the ith band integrated from the top of the atmosphere to a pressure level, p, along a slant path parallel to the solar beam.

Roach (1961) has used empirical relationships of Howard, Burch, and Williams (1956) for absorptions of individual bands of water vapor and carbon dioxide as a function of pressure and optical path. A similar approach is taken here. Howard, et al. fitted two empirical relationships to their results of a quantitative laboratory study of the molecular spectra of water vapor

and carbon dioxide from the 0.94 micron water vapor band to the 15 micron carbon dioxide band. The first of these, for weak absorption bands, is

$$A = \int A_\nu \, d\nu = cu^{\frac{1}{2}}(P + e)^k \qquad \text{for } A < A_c \; ; \tag{15}$$

and the second, for strong absorption bands, is

$$A = C + D \log u + K \log(P + e) \quad \text{for } A \geq A_c \; ; \tag{16}$$

where

ν = wave number (cm^{-1}),

A = band area in wave numbers (cm^{-1}),

A_ν = fractional absorption within a band at ν,

u = absorbing path (g cm^{-2} for H_2O; cm atm for CO_2),

e = partial pressure of the absorbing gas (mm Hg),

P = partial pressure of the non-absorbing gas (mm Hg),

p = total pressure = $P + e$,

and A_c = critical band area above which the strong absorption band expression becomes applicable. C, D, K, c, and k are empirically determined constants, utilizing eight spectral bands for water vapor absorption, and seven for carbon dioxide, allowing for the coincidence of the 2.7 band. Values for these constants are given in Table 10.

For absorption by the 9.6 μ band of ozone, Walshaw (1957) found that the band area has the form:

$$A = \int A_\nu \, d\nu = \Delta\nu[1 - 10^{-jf(\varphi)}] \; ; \tag{17}$$

where

$\Delta\nu$ = 138 cm^{-1}, the frequency range over which the band absorbs

$j = u \, \xi(u)$

u = absorbing path (cm atm for O_3)

$$\xi(u) = \begin{cases} \dfrac{1 + 0.1025u}{1 + 1.61u} & \text{for } u \leq 0.1 \\ 0.984 \times 10^{-0.53u} & \text{for } 0.1 \leq u \leq 0.4 \\ 0.317u^{-0.74} & \text{for } u \geq 0.4 \end{cases}$$

$$\varphi = \frac{u\,\xi^{a}(u)}{p}$$

$a = 2.11$

p = total pressure (mm Hg)

$$f(\varphi) = 1.185\ (1 + 734\,\varphi)^{-\frac{1}{2}}\ \eta(\varphi)$$

and $\eta(\varphi)$ = function tabulated in Table 11.

Roach (1961) points out that individual absorption lines have a temperature dependence, but errors due to neglect of absorption along vertical temperature gradients are likely to be small. However, absorption along pressure gradients cannot be neglected. Curtis (1952) suggests that this pressure dependence can be accounted for if, in Eqs. (15) and (16), it is assumed that $P >> e$, i.e., that $p = P$ and assign a value $\bar{p}$ to p given by

$$\bar{p} = \frac{\int p\ du}{\int du}\ , \tag{18}$$

where the integrations are made from the top of the atmosphere to the level concerned. This much used Curtis-Godson approximation places all the absorbing matter along a pressure gradient at one pressure, $\bar{p}$. Curtis estimated the errors introduced by this assumption to be negligible for the type of vertical distributions of water vapor and carbon dioxide in the atmosphere.

Joseph (1970) found that the albedo of the cloudless atmosphere, due to Rayleigh scattering, could be fitted to a function in $\cos\psi$. The result was the following expression:

$$\alpha_o = 0.3300e^{-1.4423 \cos\psi} + 0.2862e^{-17.4462 \cos\psi} . \quad (19)$$

Thus, the scattered part of the solar radiation reaching the earth's surface, in the absence of clouds, is (Katayama, 1972)

$$I_{o_{sfc}}^{s}(\text{clear}) = I_o^s(1 - \alpha_o)/(1 - \alpha_o\alpha_s) , \quad (20)$$

where α_s is the surface albedo, and the denominator represents a correction factor due to multiple reflection between the atmosphere and the earth's surface. Martin (1972) provides the following expression for the sea surface albedo for use in Eq. (20):

$$\alpha_s = \text{Max}\{0.06,\ 0.06 + 0.54(0.7 - \cos\psi)\} . \quad (21)$$

E. Solar Radiation - Cloudy Sky

In the case of solar radiation, clouds cannot be treated as black bodies as with infrared cooling; thus, the reflected and transmitted solar radiation must be accounted for.

The inclusion of clouds in the solar radiation scheme depends on obtaining values for absorptivity, A; transmissivity, T; and reflectivity, R, for the cloud encountered. Theoretical values of A, T, and R for low and middle clouds computed by Korb, et al., (1956) and Korb and Möller (1962) for the I_o^a part of the solar radiation were used by Kimpel (1973), and are

used in the present research for the time of year and latitude of the AMTEX experiments. These values are given in Tables 12 and 13.

Kimpel (1973) assumed that for cirrus clouds the values for absorption, transmission and reflection were constant. Following Jacobowitz's analysis (1970), it is assumed that the short wave optical thickness of the cirrus cloud may be related to the ice concentration W (gm m^{-3}) and the geometric thickness H (km) as

$$\tau \approx 40.7 \text{ WH} . \tag{22}$$

Although W and H may vary over wide limits, the product of the two does not. Fleming and Cox (1974) have derived the effects of solar radiation by cirrus ice crystals from estimates of the single scattering albedo, W_o, given by Danielson, et al., (1969). According to Fleming and Cox (1974) an absorption optical thickness τ_a and a scattering optical thickness τ_s are defined as:

$$\tau_a = (1 - W_o)\ \tau \tag{23}$$

and

$$\tau_s = W_o\ \tau . \tag{24}$$

Then, the flux transmissivity, T, reflectivity, R, and absorptivity, A, of a cirrus layer, for the I_o^a part of the shortwave radiation, are written as:

$$T = \exp(-\ \tau^* \sec\psi)$$

$$R = 1 - \exp(-\ \tau_s^* \sec\psi)$$

$$A = 1 - \exp(-\ \tau_a^* \sec\psi) , \tag{25}$$

where ψ represents the solar zenith angle. The effective optical thickness τ^* has been scaled by the parameter g of 0.875 (Van de Hulst and Grossman, 1968), so that

$$\tau^* = (1 - g)\ \tau \ . \tag{26}$$

Danielson, et al., (1969) estimate $1 - W_o \simeq 10^{-3}$ for terrestrial clouds so $W_o = 0.999$. If a model cirrus cloud is taken as having

$$H = 4 \text{ km}$$

and

$$W = .007 \text{ g m}^{-3} \ , \tag{27}$$

the expressions for transmissivity, reflectivity, and absorbtivity are finally written as:

$$T = \exp[- .142448 \sec \psi \ ] \ ,$$

$$R = 1 - \exp[- .142304 \sec \psi \ ] \ ,$$

and

$$A = 1 - \exp[- 1.42448 \times 10^{-4} \sec \psi \ ] \ . \tag{28}$$

Theoretical values for A, T, and R for cirrus clouds, as a function of solar zenith angle, are given in Table 14 for the I_o^a part of the solar radiation. These transmissivity values agree quite well with transmissivities of cirrus clouds at visible wavelengths tabulated by Kondratyev (1969) from observational data.

All I_o^a radiation reflected by clouds is considered diffuse and treated using Elsasser's (1942) 1.66 diffusion factor.

The amount of I_o^a solar radiation absorbed in a cloud is obtained from the absorptivities contained in Tables 12, 13 and

14. The further absorption of solar radiation beneath cloud bases is obtained by a procedure given by Rodgers (1967) who assumes that the spectral absorption coefficients of liquid and gaseous water are equal. Thus, an equivalent water vapor optical depth, du*, can be calculated that would yield the same value of absorption. However, the absorptivities of Tables 12, 13, and 14 apply over the full range of the solar spectrum. Thus, each absorptivity must be multiplied by (1/0.349) when determining that equivalent optical depth. Roach's clear sky technique depends on incrementing the optical path by the amount of water vapor traversed between successive pressure levels. Therefore, it is necessary to know the total optical path traversed by the beam from the top of the atmosphere through the cloud layer before the absorption below the cloud base can be computed. This is accomplished by adding du* and the optical path traversed to the cloud top. If another cloud is encountered beneath the first one, the entire process is repeated using the now diffuse solar radiation propogating downward from the bottom of the cloud above. The absorption of shortwave radiation reflected from the surface is ignored.

For the scattered part of the solar radiation, molecular scattering in clouds is negligible compared to scattering by water droplets. Absorption of the scattered part by water droplets and water vapor in clouds are neglected. Following Rodgers (1967) and Katayama (1972), the reflectivities of the scattered part of the solar radiation (R') for low, middle and high clouds are taken as 0.66, 0.54, and 0.21, respectively.

Katayama provides the following expressions for the albedo of the atmosphere for the scattered portion of solar radiation in a cloudy atmosphere:

For a single cloud layer,

$$\alpha_c = \alpha_o + (1 - \alpha_o)R_1' \ . \tag{29}$$

For 2 cloud layers,

$$\alpha_c = \alpha_o + (1 - \alpha_o)\left[1 - \frac{(1-R_1')(1-R_2')}{(1-R_1' R_2')}\right] \ . \tag{30}$$

For 3 cloud layers,

$$\alpha_c = \alpha_o + (1-\alpha_o)\left[1 - \frac{(1-R_1')(1-R_2')(1-R_3')}{1-(R_1'R_2' + R_2'R_3' + R_3'R_1') + 2R_1'R_2'R_3'}\right]. \tag{31}$$

Thus, the scattered part of the solar radiation reaching the earth's surface, in a cloudy atmosphere, is

$$I_o^s(\text{cloudy}) = I_o^s(1 - \alpha_c)/(1 - \alpha_c\alpha_s) \ . \tag{32}$$

F. Net Radiational Cooling

Using the methods previously discussed, net fluxes of solar and infrared radiation are obtained throughout the troposphere at the nineteen constant pressure surfaces. These are then converted to solar heating, infrared cooling, and net radiational cooling.

The heating and cooling, H, depends on the divergence of radiative fluxes, and can be written as

$$H = \Gamma \frac{dF}{dp} \ , \tag{33}$$

where H is in degrees centigrade, and Γ is the dry adiabatic

lapse rate (g/c_p).

G. Surface Radiation Budget

The upward long wave fluxes from the surface and at 100 mb (LW↑) and the corresponding downward fluxes (LW↓) are calculated by the technique described previously for infrared radiation. The amount of incoming solar radiation and reflected, absorbed and scattered radiation can be calculated by the methods previously discussed. Therefore, the amount of short wave radiation arriving at the surface, SW↓, is known.

The amounts of the short wave radiation components subject to absorption (Eq. 13) and subject to scattering (Eq. 12) that arrive at the surface are denoted as $SW_a\downarrow$ and $SW_s\downarrow$, respectively. These components can be further split into amounts reaching the surface through cloudy and clear sky portions of the troposphere as $SW_a\downarrow$(cloudy), $SW_a\downarrow$(clear), $SW_s\downarrow$(cloudy) and $SW_s\downarrow$(clear). These components are important in the surface budget.

The radiation budget of the ocean surface can then be written

$$Q_{r,sfc}^{(net)}\downarrow = SW_a\downarrow(\text{cloudy}) + SW_a\downarrow(\text{clear}) + SW_s\downarrow(\text{cloudy}) + SW_s\downarrow(\text{clear}) - SW_a\uparrow - SW_s\uparrow - LW_{sfc}\uparrow + LW_{sfc}\downarrow \; . \qquad (34)$$

The first four and last two terms on the right-hand side are available from calculations previously discussed. The remaining two terms are the amounts of the short wave radiation components

subject to absorption and scattering that arrive at the surface and are then reflected. These two terms can be obtained using the appropriate albedos (List, 1968 and Martin, 1972). Radiation measurements taken at the surface during AMTEX '74 are used to check the reliability of the technique developed in this research for obtaining the net radiation flux divergence term, Q_r, at the surface.

Similarly, the radiation budget at 100 mb can then be written

$$Q_{r,100}^{(net)}\uparrow = - SW_s(100)\downarrow - SW_a(100)\downarrow + SW_s(\text{scatt, clds-atm})\uparrow + SW_a(\text{refl, clds})\uparrow + SW_a\uparrow + SW_s\uparrow + LW_{100}\uparrow - LW_{100}\downarrow . \quad (35)$$

The first four and last two terms on the right-hand side of Eq. (35) are also available from the calculations discussed previously. The other two terms are obtained as they are for Eq. (34), using the same albedos. The net radiative loss by the tropospheric column can then be given as the sum of Eqs. (34) and (35) which are represented schematically in Figure 4.

CHAPTER V

RESULTS

A. Synoptic Situation During AMTEX '74

Spacial distributions of radiation budgets are examined under differing synoptic conditions which occurred during the AMTEX '74 experimental period. The AMTEX region (Figure 1) was characterized by a warm period from 14-22 February and then a cold air outbreak from 24-28 February, following a frontal passage on the 23rd.

Just prior to the experiment a cold air outbreak engulfed the region. However, by 14 February an anticyclone moved over the East China Sea and Yellow Sea. This started what was characterized as the "warm period" which lasted until the 22nd. During the warm period four weak cyclones passed over the northern part of the East China Sea and/or the Yellow Sea with a frequency of one every two to three days. These disturbances were unable to produce strong cold air advection into the AMTEX station network as the cold air masses remained to the north, passing eastward over the Sea of Japan and the Sea of Okhotsk. Each of these cyclones were followed by an anticyclone and warming. On the 22nd, a cyclone developed over the Yellow Sea and the Sea of Japan.

Strong surface ridging behind the low and accompanying cold front pushed the front into the AMTEX area, passing Naha on 23 February. This strong cold front resulted in a cold air outbreak over the region during the last five days of the experiment, 24-28 February. This was characterized as the "cold period". The major synoptic events of the AMTEX '74 period are summarized on a daily basis in Table 15 (Lenschow and Agee, 1974).

In this investigation emphasis is placed on three significant days during the AMTEX experiment. They are February 18, a warm day; February 23, the frontal passage (FROPA) day; and February 26, a cold day.

B. Time and Spacial Variations of Cloud Amounts Over the AMTEX '74 Region

Cloud conditions obtained from the 3DNEPH data varied significantly under the different synoptic conditions which occurred during the AMTEX '74 experimental period. For illustrative purposes, the mean daily amounts of total cloud cover, and low, middle and high clouds were computed at each of the thirty-six grid points circled in Figure 2 and reproduced in Figure 5. Depicted in Figures 6-9 are these mean cloud fields for 18, 23 and 26 February 1974. In addition, the amounts of cloud have been averaged over all the grid points to produce mean cloud estimates over the entire AMTEX region for each of those days. The estimates are shown in Table 16. Similar information is available for bases and tops of clouds, but is not presented

here.

On February 18 (warm day), when the anticyclone was over the East China Sea and Yellow Sea, the mean daily total cloud cover (Fig. 6) over AMTEX ranged from 0 to 71 percent. On February 23, the day of the cold frontal passage (FROPA), the total cloudiness over the region increased, ranging from 43 to 100 percent. Total cloudiness accompanying the cold air outbreak was even greater on February 26 (cold day), ranging from 53 to 100 percent. Spacially averaged total cloud amounts over the region were 33, 77 and 87 percent respectively on these three days (Table 16).

Similar spacial and daily variations can be seen in the mean daily variations of low cloud cover (Fig. 7), middle cloud cover (Fig. 8) and high cloud cover (Fig. 9). Spacially averaged low cloud amounts over the region increased from 24 percent on the warm day to 72 percent on the cold day. Likewise, the spacially averaged middle cloud amounts increased from 19 to 68 percent, and high cloud amounts increased from 8 to 30 percent between the warm and cold days (Table 16).

Inspection of cloud types (not shown here) indicated that the cloud layers were mostly stratoform on the warm day, with more cumuloform on the cold day as expected. There were considerably more low cumulus clouds on the cold day than on the warm day.

C. Comparison of Observed and Calculated Radiation Components

Initially, the methods described in Chapter IV were used to estimate radiation budgets in the column surface to 100 mb for each of the seven stations (Naze, Naha, Miyakojima, Minamidaitojima, Ryofu-maru, Keifu-maru, and Nojima) for which surface radiation flux measurements were available. The computations were carried out for February 18 (warm day), February 23 (FROPA day) and February 26 (cold day) for comparison of calculated radiation components with observed, daily-averaged values. Long wave components were computed at the four standard observation times (0300, 0900, 1500 and 2100 JST) and then averaged for each day. Since the two daylight standard observation times were the same number of hours away from local noon, the short wave components were calculated at those two times and averaged for each day.

Of the twenty-one cases examined (7 stations, times 3 days), long wave flux measurements were unavailable for four of the cases and short wave measurements were unavailable for five of the cases. A percent difference (calculated value minus measured value, divided by measured value) was evaluated for each case where a measurement was available. Quantitative results of the long wave portion of the surface flux resulting from the model developed in this research were reasonably good, with the percent difference ranging from -10.4 percent to +10.5 percent and an average percent

difference of 0.0 percent. All but two of these seventeen long wave cases had a difference equal to or less in absolute value, than 6.5 percent. Quantitative results of the short wave portion of the model were not as good, with the percent difference ranging from -28.3 percent to +331.0 percent and an average difference of +62.3 percent. For the total downward radiation at the surface (long wave plus short wave) the percent difference ranged from -6.2 percent to +18.3 percent and averaged +4.9 percent. These statistics are shown graphically in Figure 10.

From considerations of satellite resolution and mapping accuracy, and the way in which the model was constructed, the grid values of clouds used in the calculations should be treated as spacial estimates, and therefore are not necessarily representative of a particular point on earth. The magnitude of the differences seen in the verification statistics for the comparisons of estimated and measured irradiance components at a station were therefore not entirely unexpected. Further comparisons of calculated irradiance components with measured values were made to test the accuracy of the model only for those stations and times during AMTEX '74 at which the cloud values at the 3DNEPH grid point nearest the station appeared truly representative of the clouds reported on the surface synoptic and surface marine hourly observations for the same times.

Difficulties arose in determining if the 3DNEPH cloud

values and synoptic observations were compatible at a specific time and point, especially in the case of low or middle cloud overcast conditions in which case the surface observations could not provide information on the presence or absence of middle or high clouds. Also, amounts of middle and high clouds were not indicated on the surface observations. It was particularly difficult when cloud conditions were changing significantly from one hour to the next.

At Naze on 16 February at 0900 JST, Naha on 19 February at 1500 JST, and Minamidaitojima on 26 February at 0900 JST the clouds used in the model appeared representative of the clouds reported on the surface observation at a particular point (station) and time. At Naze on the 16th, the short wave radiation calculated as reaching the surface was only 0.9 percent too small, and the calculated downward flux of long wave radiation at the surface was 2.1 percent too large. At Naha on the 19th, the short wave radiation estimated as reaching the surface was 7.1 percent too large, and the estimated downward flux of long wave radiation at the surface was 3.8 percent too small. At Minamidaitojima on the 26th, the calculated short wave radiation at the surface was 9.0 percent too small, and the calculated downward flux of long wave radiation at the surface was only 1.7 percent too large.

These situations at Naze on February 16, Naha on February 19 and Minamidaitojima on February 26 tend to quantitatively

support the contention that the model developed in this research provides acceptable results when the cloud data are representative of the location where the model is applied. Since a primary use of this model is to estimate radiation budgets over a region, not at a point, and since the cloud data used are spacial estimates, the model may be applied to the examination of spacial and daily variations of atmospheric radiation over the AMTEX region.

D. Effects of Clouds on Tropospheric Radiation Budgets

To exemplify the effects of clouds, vertical profiles of radiative heating and cooling in the troposphere for a typical grid point on February 23 are displayed in Figure 11. The 0900 JST surface and upper air, and 3DNEPH data were used in the calculations. The composite cloud conditions consisted of three layers: stratocumulus (Sc) with base at 950 and top at 850 mb, altocumulus (Ac) extending from 700 to 600 mb, and cirrus (Ci) from 350 to 250 mb. Coverages were 75, 30 and 30 percent, respectively.

The irregularities in the long wave cooling profiles are coincident with the locations of the cloud layers. There is more cooling in the vicinity of the cloud tops than cloud bases. Conditions in the vicinity of the tropopause at this grid point are characterized by a slight warming. Comparatively small cooling rates or such slight warming is to be

expected near the tropopause in agreement with London (1957), Rodgers (1967) and Dopplick (1972).

To further illustrate the effects of clouds on the tropospheric and surface radiation budgets, the data at Naha on February 23 at 0900 JST were chosen. The cloud conditions at the nearest nephanalysis grid point consisted of three layers: stratocumulus (Sc) with base at 1000 and top at 900 mb, altocumulus (Ac) extending from 800 to 600 mb, and cirrus (Ci) from 450 to 250 mb. Radiative budget terms are shown in Table 17 for the clear sky and cloudiness conditions, where the cloud amounts are assumed overcast within the tropospheric column.

As is expected from radiation theory, clouds in the lower layers (Sc and Ac) increase the net radiational cooling rate of the troposphere. The opposite is true for the higher clouds (Ci). The overlapping cloud layers increase SW $rad\uparrow_{100}$ when compared to clear sky or the existence of one cloud layer. The net tropospheric cooling effect due to radiation lies between the cooling rates for each individual cloud type. The effect of all cloud layers and combinations on the surface radiation budget when compared to clear sky is to reduce SW $rad\downarrow_{sfc}$ and SW $rad\uparrow\downarrow_{sfc}$. The LW $rad\downarrow_{sfc}$ is increased with the presence of clouds. Furthermore, as is also expected from radiation theory, the clouds decrease LW $rad\uparrow_{100}$, LW $rad\uparrow\downarrow_{100}$ and $SW\uparrow\downarrow_{100}$. The introduction of clouds generally yields a reduction in NET $rad\uparrow\downarrow_{sfc}$ primarily because of increased amounts of radiation

reflected back to space. Table 17 demonstrates that cloud type and overlap are determining factors in the radiation budget at the surface. Calculations using 1975 AMTEX data show the same effects of clouds on the tropospheric radiation budgets (Kimpel and Chaplin, 1976).

Radiative heating may be manifested by many different processes in the cloud layer in which absorption takes place. These processes can include induced vertical motions, sensible heating, evaporation of cloud water, and transport of the absorbed solar energy. Also, since clouds have been shown to absorb a significant amount of solar radiation, this absorption can effect the clouds environment because absorption by clouds in a layer is much higher than for clear air.

There can be differential heating effects at the surface due to radiation. Large cumulus clouds can dramatically reduce the solar insolation reaching the surface both by reflection of the incident radiation back to space and by absorption. Thus, large differential heating at the surface between the cloud and clear air may lead to an enhancement of the temperature gradients in the horizontal.

E. Time and Spacial Variations of Atmospheric Radiation Over the AMTEX '74 Region

Next, the methods described in Chapter IV were used to estimate daily averaged radiation budgets in the column surface to 100 mb for each of the thirty-six grid points (Fig. 5).

The long wave components were computed at the four standard observation times and averaged for each day. Short wave components were calculated at the two daylight standard observation times and then averaged. These budget estimates were made for February 18 (warm day), 23 (FROPA day) and 26 (cold day).

The radiation balance at the ocean surface is composed of the six short wave components and two long wave components given in Eq. (34). The balance at 100 mb is composed of the six short wave and two long wave components given in Eq. (35). Values of these terms, estimated over the 6 by 6 grid by the radiation techniques established in this study are presented in Figures 12-33 for February 18, 23 and 26, 1974.

When the fields of radiation budget terms in Figures 12-33 are examined in light of cloudiness conditions depicted in Figures 6-9, effects of cloudiness on the spatial variations of these terms are evident. Exceptions to the following observations can and do occur due to other factors such as spacial variations in temperature and humidity profiles.

Grid point to grid point increases (or decreases) in mean daily total cloud cover (Fig. 6) generally result in respective decreases (or increases) in $LW\uparrow_{100}$ (Fig. 13) and net upward long wave fluxes (Fig. 14) at 100 mb. Conversely, grid point to grid point increases (or decreases) in mean daily total cloud cover (Fig. 6) and/or low cloud cover (Fig. 7) generally result in respective increases (or decreases)

in LW↓ at the surface (Fig. 15). The effect of LW↑ at the surface (Fig. 16) due to varying sea surface temperatures (not shown) appears more pronounced than cloud effects on the net upward long wave fluxes at the surface (Fig. 17).

The amount of the short wave radiation component subject to absorption that is reflected by the clouds (Fig. 19) and the amount of the short wave radiation component subject to scattering that is scattered upward by the clouds and atmosphere (Fig. 23) increase with increasing total cloudiness (Fig. 6) as expected. The amounts of the short wave radiation components subject to absorption and scattering that are reaching the surface through clouds (Figs. 20 and 24) increase with increasing total clouds (Fig. 6) as the amounts of these components reaching the surface through clear portions of the sky (Figs. 21 and 25) similarly decrease.

Clouds in the lower layers (Fig. 7) have an influence on the spacial variation of long wave cooling (Fig. 31) and net radiational cooling (Fig. 33) rates. In most instances these rates increase from grid point to grid point with corresponding increases in amounts of low cloud cover. However, the low cloud effect is not as systematic on the spacial variations of these fields as total cloud cover is on other fields because of effects of overlapping cloud layers and cloud type (Ref. Sec. D).

These relationships between radiation budget terms (Figs. 12-33) and cloud conditions (Figs. 6-9) demonstrate that spacial variation in cloudiness in addition to cloud type and overlap (Sec. D), are determining factors in the radiation budgets in

the troposphere and at the surface. This and the possible effects of clouds on vertical and horizontal temperature gradients due to radiation point out that realistic modeling of spacial variations of radiative fluxes such as provided by the model developed in this research are essential for studies of topics such as convection, energetics and air mass transformation and general circulation.

The grid fields of radiation terms presented in Figures 12-33 have been averaged over the grid and are depicted in Figures 34(a), (b), and (c) for February 18, 23, and 26, respectively. In addition, Table 18 summarizes the mean radiation budget of the troposphere (surface to 100 mb on these three days).

The average net radiative loss by the atmospheric column was larger during the warm day than the cold day. This suggests that the net radiative contribution to air mass modification is a reduction in cooling, or possibly even warming over the region. Therefore, daily variations, in addition to spacial variations, in radiation components should prove valuable in studying air mass transformation, and heat and energy budgets in the AMTEX region.

Ninomija (1974, 1975) has reported on the mean heat energy budget during AMTEX '74. He used the aerological data at standard pressure levels with a time interval of 12 hours. However, as pointed out by Nitta (1976), the influence of air mass transformation is mainly confined in the lower layer below 800 mb

and the standard level data seem to be too crude to resolve detailed processes of air mass transformation. The vertical resolution of 50 mb and time interval of 6 hours used in this study are better suited for use in heat and moisture budget studies. Furthermore, Ninomija used a climatological value of radiation heating rate on a vertical cross section along 30°N latitude circle for January as presented by Katayama (1966). The climatological value is not appropriate to use due to varying synoptic and cloud conditions over the AMTEX area. The use of 3DNEPH data, the refinement of vertical resolution, and radiative heating rates averaged over four times a day in this study should provide better estimates of radiation heating rates.

The radiative heating is an important parameter for a heat budget. Although the radiative heating may have a small effect on the whole budget during the period of cold-air outbreaks as reported by Manabe (1957, 1958) and Ninomija (1972), the computation of the vertical distribution of eddy heat fluxes depends on the distribution of radiative heating. When the heat supply from the surface is not very large, the estimation of radiative heating is especially important for the heat and moisture budgets (Yanai et al., 1973, and Nitta and Esbensen, 1974). Since the vertical distributions of radiative heating over the AMTEX area vary according to location and different synoptic situations, it is essential that daily radiative heating be calculated by a model such as

developed in this research rather than using climatological values or coarse vertical resolution.

It is difficult to compare the budgets presented here with the results of other studies because of the unique use of the US Air Force Global Weather Central, 3-Dimensional Nephanalysis data in the estimates of spacial variations of radiative transfer. The net tropospheric cooling rates of 0.941 $^{\circ}C\ day^{-1}$, 0.981 $^{\circ}C\ day^{-1}$ and 0.711 $^{\circ}C\ day^{-1}$ for February 18, 23, and 26 are within 4.5 percent, 9.0 percent and 21.0 percent, respectively of the the net cooling rate obtained by Dopplick (1972) for the latitude area and season of AMTEX. However, Dopplick's results are seasonal, zonal mean heating rates that are not necessarily representative of particular times or geographic regions such as the oceanic areas of AMTEX. Significant variations in radiational cooling rates can result from day to day, and grid point to grid point as can be seen in the cases examined in this study.

The SW $rad\downarrow_{100}$ and SW $rad\uparrow_{100}$ components given in Table 18 allow for an estimate of the effective albedo at 100 mb. Values are 0.36, 0.56, and 0.59 for February 18, 23, and 26, respectively. These vary primarily as results of differences in cloudiness.

CHAPTER VI

SUMMARY AND RECOMMENDATIONS

The main purpose of this research is to develop a radiation model that provides realistic results for radiative transfer in a cloudy atmosphere. Kimpel's (1973) technique is improved upon to include: (1) the use of the US Air Force Global Weather Central, three-dimensional nephanalysis (3D-NEPH) data (Coburn, 1971) in a unique estimate of radiative transfer, (2) better treatment of Rayleigh scattering by air molecules and water vapor (Joseph, 1971), (3) multiple reflections of radiation between cloud layers for the scattered part of solar radiation (Katayama, 1972), (4) more adequate treatment of stratospheric radiative transfer by water vapor, carbon dioxide and ozone; and (5) the incorporation of water vapor emissivities adapted from Staley and Jurica (1970).

Data from the 3DNEPH and six-hourly upper-air observations of temperature and humidity are entered into the radiation model developed in this research. Through the long and short wave methods described in Chapter IV, net fluxes of solar and infrared radiation are obtained throughout the troposphere at nineteen constant pressure levels. These are then converted to solar heating, long wave cooling and net

radiational cooling rates. These methods also allow the estimation of tropospheric and surface radiation budgets.

Results tend to quantitatively support the contention that the model developed in this research provides acceptable results when the cloud data are representative of the location where the model is applied. Since a primary use of this model is to estimate radiation budgets over a region, not at a point, and since the cloud data used are spacial estimates, it is reasonable to apply the model to the examination of spacial and daily variations of atmospheric radiation over the AMTEX region.

Calculations using the model developed in this research show that the average net radiative loss by the atmospheric column in the AMTEX '74 area was larger during the warm day (February 18, 1974), than the cold day (February 26, 1974). This suggests that the net radiative contribution to air mass modification is a reduction in cooling, or possibly even warming over the region.

The net tropospheric cooling rates of 0.941 $^{\circ}C\ day^{-1}$, 0.981 $^{\circ}C\ day^{-1}$, and 0.711 $^{\circ}C\ day^{-1}$ for February 18, 23, and 26, 1974 are within 3.9 percent, 3.8 percent and 24.0 percent respectively of the net cooling rate obtained by Dopplick (1972) for the latitude area and season of AMTEX. However, Dopplick's seasonal, zonal mean heating rates are not necessarily representative of particular times or geographic regions such as the oceanic areas of AMTEX. Results of cases examined in this study show that significant variations in radiational cooling

rates can result from day to day, and grid point to grid point, primarily due to cloud effects.

Calculations demonstrate that cloud overlap and type are determining factors in the radiation budgets in the troposphere and at the surface and have significant effects on the vertical profiles of radiative heating and cooling.

It appears that clouds are the primary determining factor in providing realistic values for radiative transfer in the troposphere. The 3DNEPH data provides, for the first time, a means of incorporating representative cloud conditions in examining spacial and daily variations of radiation parameters.

Results from this study are related to broader objectives of AMTEX. The model developed in this research provides upward and downward radiant fluxes near the ocean surface which are required for study of boundary layer processes and energy budgets.

Several promising areas for continued research result from this investigation. Research should continue on the application of the US Air Force Global Weather Central 3DNEPH data. The radiation model and 3DNEPH data might be used to experimentally determine more representative values of short wave absorptivity, transmissivity and reflectivity values, and effective long wave emissivities of different cloud types.

The computational scheme used in the calculations of this research can only accommodate three layers of clouds (low, middle, and high). Ways of including more layers of 3DNEPH

data should be investigated.

Radiative fluxes and temperature changes resulting from the model provided in this research could enable the study of the influence of radiation on convection and the investigation of the extent to which convection is induced and enhanced by radiation.

This research provides realistic modeling of radiation fluxes for the use of oceanographers, providing them with components essential for air-sea interaction studies.

It is known that radiation is the primary energy source for the generation and maintenance of atmospheric motion and the development of global circulation systems (Lorenz, 1967). But, the mutual interaction between fields of motion and radiation is so complicated that it is not fully understood. Improved parameterization of radiation fields will aid researchers in determining the interaction, and in improving numerical models of global circulation.

There will be a continuing need for investigation and development of simplified methods of radiation calculations in the solar and terrestrial spectrum. Experimental and empirical treatment of clouds need continued attention, i.e., the development of empirical relations between cloud and various radiation parameters.

Radiation experiments are also basic to the improvement of dynamic models. Diabatic heating rates due to radiation can be calculated for inclusion of thickness tendencies and

vorticity contributions in forecast models.

Gille and Krishnamurti (1972) have looked at the role of long wave radiative cooling during the passage of an easterly wave in a tropical prediction model. The motivation of their study was to see if the energetics were altered by the inclusion of long wave radiative effects. They found that the energetics were changed in such a way as to restore the conditional instability, thereby working against the stabilizing influences of the vertical eddy flux of moisture. The results indicated an important role of differential radiative cooling for short range numerical weather prediction over the tropics. The effect may not be as important in middle latitudes. This should be investigated, as should the effects of including short wave radiative warming.

The model developed in this research does not lend itself to real time operational use at present because of the time and computer storage required to carry out the calculations. The model has been run on an IBM 370-158 computer and takes approximately 213,500 bytes of storage space. Estimations of the radiative terms in the column surface to 100 mb, using the methods described in Chapter IV, for all 36 grid points at the four standard observation times, takes about 71 minutes of CPU time or nearly 30 seconds per grid point. Continued effort should be made not only to improve the radiative techniques used in the model, but also to develop increasingly efficient algorithms.

BIBLIOGRAPHY

Allen, C. W., 1958: Solar radiation. Q. J. Roy. Meteor. Soc., 84, 307-318.

Amburn, S. A., 1976: Estimates of sensible and latent heat transfer at the air-sea interface during AMTEX '74. M.S. Thesis, The University of Oklahoma, Norman, 126 pp.

Barnes, S. L., 1973: Mesoscale objective map analysis using weighted time - series observations. NOAA Tech. Memo. ERL NSSL-62, 60 pp.

Baur, F. and H. Philipps, 1934, 1935: Der Wärmehaushalt der Lupthülle der Nordhalbkuget im Januar and Juli zur Zeit der Aquinoktien und Solstitien. Gerl. Beitr. Z. Geophys., 41, 160-207; 45, 82-132.

Budyko, M. I., Editor, 1963: Atlas Teplovogo Balansa Zemnogo Shara (Atlas of the Heat Balance of the Earth), Mezdure-domstrennyT GeofizicheskiT Komitet pri Prezidiume, Moscow, U.S.S.R. Academy of Sciences, 69 pp.

Coburn, A. R., 1971: Improved three dimensional nephanalysis model. AFGWC Tech. Memo. 71-2. Air Force Global Weather Central, AWS (MAC), Offutt AFB, Nebraska, 68113, 72 pp.

COESA, 1962: U.S. Standard Atmosphere, 1962. U.S. Govt. Printing Office, Washington, D.C., 278 pp.

Craig, R. A., 1965: Physics of the Upper Atmosphere. Pergamon Press, 365 pp.

Curtis, A. R., 1952: Discussion of a statistical model for water-vapour absorption. Q. J. Roy. Meteor. Soc., 78, 638-640.

Danielson, R. E., D. R. Moore and H. C. Van de Hulst, 1969: The transfer of visible radiation through clouds. J. Atmos. Sci., 26, 1078-1087.

Davis, P. A., 1963: An analysis of the atmospheric heat budget. J. Atmos. Sci., 20, 5-22.

Dopplick, T. G., 1972: Radiative heating of the global atmosphere. J. Atmos. Sci., 29, 1278-1294.

Elsasser, W. M., 1938: On some properties of the water vapor spectrum and their relations to atmospheric radiation. Mon. Wea. Rev., 65, 323-326.

_____, 1942: Heat transfer by infrared radiation in the atmosphere. Harvard Meteorological Studies. No. 6, Blue Hill Meteorological Observatory, 105 pp.

_____, 1960: Atmospheric Radiation Tables. Amer. Meteor. Soc., Boston, Monograph 23, 43 pp.

Fleming, J. R., and S. K. Cox, 1974: Radiative effects of cirrus clouds. J. Atmos. Sci., 31, 2182-2188.

Gandin, L. S., 1965: Objective Analysis of Meteorological Fields. Israeli Program for Scientific Translations, Jerusalem, 242 pp.

Gille, J. C. and T. N. Krishnamurti, 1972: On radiative interactions in a tropical disturbance. Preprints Conf. Atmospheric Radiation, Ft. Collins, Colo., Amer. Meteor. Soc., 266-268.

Goody, R. M., 1964: Atmospheric Radiation. Oxford University Press, 436 pp.

Houghton, H. G., 1954: On the annual heat balance of the northern hemisphere. J. Meteor., 11, 1-9.

Howard, J. N., D. E. Burch and D. Williams, 1956: Near infrared transmission through synthetic atmospheres. J. Opt. Soc. Am., Nos. 3, 4, 5, p. 452.

Humphreys, W. J., 1940: Physics of the Air. McGraw-Hill Book Co., New York, 676 pp.

Jacobowitz, H., 1970: Emission, scattering and absorption of radiation in cirrus cloud layers. Ph.D. Thesis, Massachusetts Institute of Technology, 181 pp.

Joseph, J. H., 1971: On the calculation of solar radiation fluxes in the troposphere. Solar Energy, 13, 251-261.

Katayama, A., 1966: On the radiation budget of the troposphere over the northern hemisphere (I). J. Meteor. Soc. Japan, 44, No. 6, 381-401.

_____, 1967a: On the radiation budget of the troposphere over the northern hemisphere (II). J. Meteor. Soc. Japan, 45, No. 1, 1-25.

_____, 1967b: On the radiation budget of the troposphere over the northern hemisphere (III). J. Meteor. Soc. Japan, 45, No. 1, 26-38.

_____, 1972: A simplified scheme for computing radiative transfer in the troposphere. Numerical Simulation of Weather and Climate, Tech. Report No. 6, Dept. of Meteorology, University of California, Los Angeles, 77 pp.

Kimpel, J. F., 1973: On the heat budget of the summer troposphere over the tropical western pacific. Ph.D. Dissertation, Madison, University of Wisconsin, 102 pp.

_____, 1975: Objective cloud analyses used in radiation calculations during AMTEX '74. Preprints, 4th AMTEX Study Conference, Meteor. Research Inst., Tokyo, Japan, 31-34.

_____, and W. H. Chaplin, Jr., 1976: Cloud distributions and radiation fields during AMTEX. AMTEX Work Shop, November 8-9, 1976, Tokyo, Japan, 13 pp.

Kondratyev, K. Ya., 1969: Radiation in the Atmosphere. Academic Press Inc., New York, New York, 912 pp.

_____, 1972: Radiation Processes in the Atmosphere. Second IMO Lecture, WMO-No. 309, Geneva, World Meteorological Organization, 214 pp.

Korb, G., J. Michalowsky and F. Möller, 1956: Investigations on the heat balance of the troposphere. Tech. Report No. 1, contract AF 61 (S 14) - 863, University of Mainz, Germany, 93 pp.

Korb, G. and F. Möller, 1962: Theoretical investigations of energy gain by absorption of solar radiation in clouds. Final Tech Report, Contract DA-91-591-EUC-1612, University of Munich, Germany, 185 pp.

Kuhn, P. M., 1962: Radiometersonde measurements of water vapor flux emissivity. Ph.D. Dissertation, Madison, Univ. of Wisconsin, 62 pp.

_____, 1963: Radiometersonde observation of infrared flux emissivity of water vapor. J. Appl. Meteor., 2, 368-378.

Lenschow, D. H. and E. M. Agee, 1974: The air mass transformation experiment (AMTEX): preliminary results from 1974 and plans for 1975. Bull. Amer. Meteor. Soc., 55, 1228-1235.

List, Robert J., 1968: Smithsonian Meteorological Tables. Smithsonian Miscellaneous Collections, Vol. 114, 6th Ed., 527 pp.

London, J., 1957: A study of the atmospheric heat balance. Final Report on Contract AF 19 (122)-165. New York University, 99 pp.

Lorenz, E. N., 1967: The nature and theory of the general circulation of the atmosphere. WMO, No. 218, 115 pp.

Manabe, S., 1957: On the modification of air mass over Japan Sea when the outburst of cold air predominates. J. Meteor. Soc. Japan, 35, 311-326.

_____, 1958: On the estimation of energy exchange between the Japan Sea and the atmosphere during winter based upon the energy budget of both the atmosphere and the sea. J. Meteor. Soc. Japan, 36, 123-133.

_____ and F. Möller, 1961: On the radiative equilibrium and heat balance of the atmosphere. Mon. Wea. Rev., 89, 508-532.

Martin, F. L., 1972: Description of a Radiation Package for the Naval Postgraduate School General Circulation Model. Naval Postgraduate School, Monterey, CA, 51 pp.

McClatchey, R. A., R. W. Fenn, J. E. A. Selby, F. E. Volz, and J. S. Garing, 1972: Optical properties of the atmosphere (third edition), Environmental Research Papers, No. 411, AFCRL-72-0497, Cambridge Research Laboratories, L. G. Hanscom Field, Bedford, Massachusetts, 01730, 113 pp.

Möller, F., 1935: Die Wärmequellen in der freien atmosphere. Meteorol. Z., 52, 408-412.

_____, 1943: Das Strahlungsdiagramm. Reichsamt für Wetter dienst Berlin.

Mügge, R. and F. Möller, 1932: Zur berechnung von strahlungsströmen und temperaturänderungen in atmosphären von beliebigem aufbau. Zert Geophys., 8, 53-64.

Ninomiya, K., 1972: Heat and water vapor budget over the East China Sea in the winter season. J. Meteor. Soc. Japan, 50, 1-17.

_____, 1974: Note on synoptic situation and heat energy budget during the AMTEX '74. J. Meteor. Soc. Japan, 52, 452-455.

_____, 1975: Large-scale aspects of air-mass transformation over the East China Sea during AMTEX '74. J. Meteor. Soc. Japan, 53, 285-303.

Nitta, T., 1976: Large-scale heat and moisture budgets during the air mass transformation experiment. J. Meteor. Soc. Japan, 54, 1-14.

_____ and S. Esbensen, 1974: Heat and moisture budget analysis using BOMEX data. Mon. Wea. Rev., 102, 17-28.

Petterssen, S., 1956: Weather Analysis and Forecasting. McGraw-Hill, Inc., 428 pp.

Reynolds, D., 1973: Absorption of solar radiation in the tropics and its effects on mesoscale activity. M.S. Thesis, Colorado State University, Atmos. Sci. Dept., 75 pp.

Reynolds, D. W., T. H. Vonder Harr, and Stephen K. Cox, 1975: The effect of solar radiation absorption in the tropical troposphere. J. Appl. Meteor., 14, 433-444.

Roach, W. T., 1961: The absorption of solar radiation by water vapor and carbon dioxide in a cloudless atmosphere. Q. J. Roy. Meteor. Soc., 87, 364-373.

Robinson, G. D., 1950: Notes on the measurement and estimation of atmospheric radiation. Q. J. Roy. Meteor. Soc., 76, 37-51.

Rodgers, C. D., 1967: The radiative heat budget of the troposphere and lower stratosphere. Planetary Circulations Project Report No. A2, Dept. of Meteorology, Mass. Inst. Tech., 99 pp.

Sasaki, Y., 1971: A theoretical interpretation of anisotropically weighted smoothing on the basis of numerical variational analysis. Mon. Wea. Rev., 99, 698-708.

Schmidt, F., 1939: Über die absorption von wasserdampf and kohlenbhängigkeit. Beitr. Z. Geophys., 54, 203-234.

Simpson, G. C., 1928: Further studies in terrestrial radiation. Mem. Roy. Meteor. Soc., 3, No. 21, 1-26.

Staley, D. O., and G. M. Jurica, 1970: Flux emissivity tables for water vapor and carbon dioxide. J. Appl. Met., 9, 365-372.

Tousey, R., and E. O. Hulbert, 1945: Brightness and polarization of the daylight sky at various altitudes above sea level. J. Opt. Soc., 37, 78-92.

Van de Hulst, H. G., and K. Grossman, 1968: Multiple light scattering in planetary atmospheres. The Atmospheres of Venus and Mars. New York, Gordon and Breach.

Walshaw, C. D., 1957: Integrated absorption of the 9.6 μ band of ozone. Quart. J. Roy. Meteor. Soc., 83, 315-321.

Yamamoto, G., 1952: On a radiation chart. Sci. Rep. Tohoku Univ. Ser. 5, Geophysics, 4, 9-23.

_____, 1953: Radiative equilibrium of earth's atmosphere. I. The grey case. Sci. Rep. Tohoku Univ. Ser. 5, Geophysics, 5, 45-57.

Yanai, M. S., S. Esbensen and J. H. Chu, 1973: Determination of bulk properties of tropical cloud clusters from large-scale heat and moisture budgets. J. Atmos. Sci., 30, 611-627.

APPENDIX A

CLOUD ANALYSIS MODEL

The Air Force Global Weather Central (AFGWC) three dimensional nephanalysis (3DNEPH) model (Coburn, 1971) produces high resolution, three dimensional analyses of clouds in the atmosphere. A horizontal grid spacing of approximately 25 nautical miles is used. Analyses are made for 15 layers from the earth's surface to 55,000 feet MSL. The levels are variable in thickness to provide increased resolution near the surface, with 150 feet depth for layer 1 and 20,000 feet depth for layer 15. The first 6 levels are referenced to the surface so they, in effect, are terrain following. The remaining 9 levels are fixed with respect to sea level and correspond to significant meteorological pressure heights. Table A-1 provides information on the bases and tops of the 15 layers. The 3DNEPH program is run every 3 hours in the Northern Hemisphere.

The 3DNEPH analysis begins with a continuity field which consists of the previous nephanalysis. All new data are then added to this continuity field. Such a procedure precludes the omission of large areas where data may not be currently available. The next step is to incorporate various data types.

A surface data processor computes total cloud amounts plus

layered cloud amounts from validated surface reports, including layered cloud data extracted from surface reports transmitted in SYNOP, METAR, and AIRWAYS codes; present weather; total sky cover; amount of all low (or middle) clouds present; types of low, middle and high clouds; and the height above ground of the base of lowest cloud seen.

The RAOB and aircraft data processors compute layered cloud amounts from upper air reports and validated aircraft reports.

A manual data processor permits manual insertion of data as a substitute for surface reports, or as corrective "override" data in areas of missing or erroneous data. "Override" data will be ranked higher than any other type of data processed by the 3DNEPH program.

A decision tree processor then integrates all of the cloud information obtained from the previously described processors. The 3DNEPH program assigns each surface report to the nearest grid point. In order for two or more surface reports to be assigned to the same grid point, they must be located within a 15 nautical miles radius of the grid point. The density of reporting stations throughout the world is such that this condition occurs very infrequently. When this does occur an objective decision is made as to which report is used. Data from surface reports are assigned the highest ranking of conventionally-sensed data, except for layers above 10,000 ft MSL, for which data from aircraft reports are ranked higher. Data from

aircraft reports are then assigned to grid points, replacing any surface data for layers above 10,000 ft. Data from RAOBS are subsequently stored only for those elements which have not been affected by surface or aircraft reports.

The integrated "best reports" from the decision processor are stored for further processing with satellite data.

The satellite video and infrared data processors numerically convert raw satellite brightness and radiance values into meaningful cloud data for the 3DNEPH program. The video data processor performs the following six essential functions:

(1) Digitization of voltage responses of the radiance from the field of view.

(2) Statistical processing.

(3) Gross error check to detect and reject cloud data incorrectly specified either with respect to position over the earth's surface or with respect to acceptable brightness values. This check is accomplished by comparing the cloud analysis from the satellite data against a 3DNEPH analysis from other observations taken within 3 hours of the satellite data time.

(4) Update of the cloud-free background brightness fields.

(5) Gray shade (brightness values) to cloud amounts conversion.

(6) Decisions within the processor. Data are ranked according to timeliness and data source. Satellite

video data provide only two types of information, total cloud coverage and type of cloud. If satellite data are timely (less than 2 hours old), they are used to determine total coverage. There is one exception to this rule; if the total coverage reported by the satellite is less than 4/8, current conventional data will override the satellite data.

The satellite infrared data processor performs seven functions:

(1) Statistical treatment of the data.

(2) Analysis of the surface temperature field.

(3) Corrections for atmospheric attenuation.

(4) Conversion of the temperature of the radiating surface (cloud top or ground) to heights.

(5) Calculation of total cloud coverage.

(6) Gross error check of the data. This check is similar to that for the video data except that 80% correlation with surface data are required.

(7) Merging of infrared data with other types of data and the continuity field to produce the high resolution cloud analysis.

A final processor makes the final determination of the relative importance of the various types of data, i.e. the continuity fields, the integrated "best reports," and the satellite data. At this point, the 3DNEPH program has completed its analysis for the fifteen levels. The analysis provides 22

parameters at each grid point. These are total cloud amount (percent); minimum base (feet above ground level); maximum top (feet above ground level); a coded value representing surface present weather; low, middle, and high cloud type (coded value); and percent coverage for each of the 15 layers.

Since the computational scheme used (Kimpel, 1973) in the calculation of the radiation budgets can only accommodate three layers of clouds (low, middle, and high), the fifteen layers of 3DNEPH data have to be combined into a composite three layer cloud analysis, including cloud type, base, top and amount for each layer.

The base of the low cloud layer, for this composite three layer analysis, is taken as the minimum base of the first eight layers of the 3DNEPH analysis. The top of the low cloud layer is then taken as the maximum top of the first eight layers of the 3DNEPH analysis. Thus, the base of the composite low cloud layer is between the surface and 5000 feet, and the top between 150 and 6500 feet. The amount of sky covered by the low cloud layer is taken as the average amount of coverage in those layers of the first eight levels of the 3DNEPH analysis containing clouds. The composite middle and high cloud information are formed in a similar manner. The base of the composite middle cloud layer is between 6501 and 18001 feet, and the top between 10,000 and 22,000 feet. The base of the composite high cloud layer is between 22,001 and 35,001 feet, and the top between 26,000 and 55,000 feet. Cloud bases and tops are then fitted

to the nearest 50 mb constant pressure level.

This composite analysis is accomplished over a rectangular (21 x 22) grid, with a horizontal spacing of approximately 46.3 km, enclosing the AMTEX network. From consideration of the way in which the cloud model is constructed, the grid values should be treated as spacial estimates, and therefore are not necessarily representative of a particular point on the earth.

Figure A-1 depicts the information available for this composite three layer spacial estimate at a typical grid point in the AMTEX region, on February 23, 1974, at 0900 Japan Standard Time (JST). The cloud conditions consist of three layers: stratocumulus (Sc) with base at 950 and top at 850 mb, altocumulus (Ac) extending from 700 to 600 mb, and cirrus (Ci) from 350 to 250 mb. Coverages are 75, 30 and 30 percent respectively. The total amount of sky covered by cloud is 89 percent. Similar information is input at all the grid points for inclusion in the radiation computations.

For radiation calculations it is necessary to know how the three cloud layers are distributed in the troposphere. With three cloud layers and a portion of clear sky, there are eight possible situations that a stream of radiant energy might encounter as it passes vertically through the atmosphere. This is shown schematically in Figure A-2. With the amount of sky covered by each cloud layer known, and assuming a random distribution of clouds in the vertical, the probability of encountering each of the eight cloud situations can be obtained.

If the cloud distribution is indeed random, then the probability of encountering no clouds, P(8), should equal the amount of clear sky obtained from actual observations. However, this condition is rarely met. It was necessary, then to use a system whereby the observed clear sky amounts were preserved (Kimpel, 1973). In addition it was decided that such a vertical cloud arrangement should pertain only to opaque cloud amounts. Optically thin clouds, though important, have a lesser effect on the tropospheric radiation budget which could not be deduced from observations and techniques presently available. To accomplish these goals, a weighting factor, w, was defined by

$$w = \frac{T_{co}}{\sum_{i=1}^{7} P(i)}$$

where T_{co} is the average portion of the sky covered by opaque clouds. If P(1) through P(7) are multiplied by the weighting factor, their sum is T_{co} and P(8) can thus be set equal to $(1.0-T_{co})$. Use of the weighting factor has the effect of changing the cloud amounts at each of the three layers by a constant ratio so that the new distribution in the vertical preserves the measured clear sky amount and the measured total opaque cloud amount. The resulting sets of overlapping cloud parameters are inserted into the radiation schemes.

Table 1. List of Japan Meteorological Agency stations used in this study.

STATION	LAT	LONG	INT' NAT. ST. NO.	HT. OBS. SITE ABOVE SEA LEVEL
Naha	26°12'N	127°40'E	47936	29.1 m
Naze	28°23'N	129°33'E	47909	295.0 m
Minamidaitojima	25°50'N	131°14'E	49945	15.7 m
Nojima	23°30'N	128°00'E	Research Vessel	5.3 m
Ishigakijima	24°20'N	124°10'E	47918	7.2 m
Keifu Maru	28°00'N	125°00'E	Research Vessel	8.0 m
Ryofu Maru	29°30'N	127°00'E	Research Vessel	5.7 m
Miyakojima	24°47'N	125°17'E	47927	39.2 m
Kagoshima	31°38'N	130°36'F	47827	282.6 m

Table 2. Stratospheric vertical distribution of ozone (Craig, 1965) and temperature (COESA, 1962) used in radiation flux calculations.

Pressure (mb)	Temperature (°K)	Ozone Optical Depth Increment (atm cm)
50.0	215.2	0.012
45.0	215.2	0.015
40.0	215.2	0.020
35.0	215.2	0.030
30.0	215.2	0.030
25.0	215.2	0.030
20.0	215.2	0.030
15.0	217.4	0.020
10.0	218.0	0.010
7.0	223.0	0.007
5.0	227.8	0.005
3.0	235.0	0.001
2.0	243.5	0.002
1.0	264.5	0.0
0.6	265.7	0.0
0.3	271.0	0.0
0.1	233.0	0.0

Table 3. Carbon dioxide flux emissivity as a function of optical depth, u, and temperature (Staley and Jurica, 1970).

u_{CO2}(atm cm)	log u_{CO2}	Emissivity (percent) -70C	-40C	-10C	+20C
.0001	-4.0	0.114	0.119	0.115	0.108
.0002	-3.7	0.162	0.171	0.167	0.158
.0005	-3.3	0.247	0.262	0.260	0.248
.001	-3.0	0.331	0.354	0.352	0.338
.002	-2.7	0.439	0.471	0.471	0.454
.005	-2.3	0.641	0.691	0.693	0.672
.01	-2.0	0.859	0.928	0.934	0.907
.02	-1.7	1.19	1.29	1.30	1.27
.05	-1.3	1.92	2.08	2.11	2.07
.10	-1.0	2.78	3.03	3.08	3.03
.20	-0.7	3.92	4.30	4.39	4.32
.50	-0.3	5.76	6.36	6.54	6.49
1.0	0.0	7.19	7.99	8.26	8.23
2.0	0.3	8.60	9.61	10.0	10.0
5.0	0.7	10.40	11.71	12.3	12.4
10.0	1.0	11.7	13.3	13.9	14.1
20.0	1.3	13.0	14.8	15.6	15.8
50.0	1.7	14.7	16.7	17.7	18.0
100.0	2.0	15.9	18.1	19.3	19.6
200.0	2.3	17.0	19.5	20.7	21.1
500.0	2.7	18.6	21.3	22.7	23.1
1000.0	3.0	19.7	22.6	24.1	24.4
2000.0	3.3	20.7	23.9	25.4	25.7

Table 4. Water vapor flux emissivity as a function of optical depth, u, and temperature (Staley and Jurica, 1970).

u_{H_2O}(pr cm)	log u_{H_2O}	Emissivity (percent) -70C	-40C	-10C	+20C
.00001	-5.0	2.16	1.9	1.86	1.96
.00002	-4.7	3.16	2.72	2.58	2.62
.00005	-4.3	5.11	4.4	4.11	4.09
.0001	-4.0	7.16	6.16	5.72	5.65
.0002	-3.7	9.77	8.41	7.81	7.68
.0005	-3.3	14.1	12.2	11.4	11.2
.001	-3.0	18.0	15.7	14.6	14.3
.002	-2.7	22.3	19.6	18.3	18.0
.005	-2.3	28.3	25.1	23.6	23.2
.01	-2.0	32.6	29.2	27.7	27.3
.02	-1.7	36.8	33.3	31.9	31.6
.05	-1.3	42.2	38.8	37.4	37.3
.10	-1.0	46.2	42.8	41.7	41.8
.20	-0.7	50.2	47.1	46.2	46.5
.50	-0.3	56.0	53.4	52.9	53.6
1.0	0.0	61.1	59.1	59.0	60.0
2.0	+0.3	67.3	66.2	66.6	67.7
5.0	+0.7	77.4	77.8	78.8	79.8
10.0	+1.0	85.3	86.8	88.1	88.8
20.0	+1.3	91.5	93.8	95.1	95.4
50.0	+1.7	95.6	98.0	98.8	98.7

Table 5. Ozone flux emissivity as a function of optical depth, u, and temperature (Staley and Jurica, 1970).

u_{O_3} (atm cm)	log u_{O_3}	Emissivity (percent) -70C	-40C	-10C	+20C
.0001	-4.0	0.109	0.155	0.191	0.214
.0002	-3.7	0.167	0.239	0.300	0.340
.0005	-3.3	0.284	0.412	0.520	0.594
.001	-3.0	0.415	0.610	0.777	0.896
.002	-2.7	0.588	0.872	1.12	1.29
.005	-2.3	0.900	1.34	1.72	1.99
.01	-2.0	1.20	1.79	2.30	2.68
.02	-1.7	1.53	2.31	2.99	3.51
.05	-1.3	1.99	3.03	3.97	4.71
.10	-1.0	2.30	3.54	4.66	5.55
.20	-0.7	2.59	4.01	5.30	6.33
.50	-0.3	2.97	4.60	6.10	7.29
1.0	0.0	3.24	5.02	6.64	7.93
2.0	+0.3	3.47	5.36	7.08	8.43
5.0	+0.7	3.71	5.68	7.47	8.84
10.0	+1.0	3.83	5.84	7.65	9.03

Table 6. Flux emissivity correction quantity for water vapor-carbon dioxide overlap at -70C. Multiply values in table by 10^{-4} (Staley and Jurica, 1970).

log u_{CO_2}	log u_{H_2O}																
	−3.7	−3.3	−3.0	−2.7	−2.3	−2.0	−1.7	−1.3	−1.0	−0.7	−0.3	0.0	0.3	0.7	1.0	1.3	1.7
−4.0	0	0	0	0	0	0	0	0	0	1	1	2	4	6	8	9	10
−3.7	0	0	0	0	0	0	0	0	0	1	2	3	5	9	11	12	13
−3.3	0	0	0	0	0	0	0	0	1	1	3	5	8	13	17	19	20
−3.0	0	0	0	0	0	0	0	0	1	2	4	7	11	18	22	25	27
−2.7	0	0	0	0	0	0	0	0	1	2	5	9	14	24	30	33	36
−2.3	0	0	0	0	0	0	0	1	2	3	7	13	21	34	43	48	52
−2.0	0	0	0	0	0	0	0	1	2	4	10	17	28	46	58	65	70
−1.7	0	0	0	0	0	0	0	1	3	6	14	24	39	63	80	90	97
−1.3	0	0	0	0	0	0	1	2	5	9	22	38	62	101	128	144	156
−1.0	0	0	0	0	0	1	1	3	7	14	31	55	89	146	184	208	226
−0.7	0	0	0	0	0	1	2	4	10	19	44	77	124	204	258	292	319
−0.3	0	0	0	0	1	1	2	7	14	28	64	111	180	297	376	426	467
0.0	0	0	0	0	1	1	3	8	17	35	80	137	222	366	465	528	581
0.3	0	0	0	0	1	2	3	10	21	41	94	162	262	432	550	628	692
0.7	0	0	0	0	1	2	4	12	25	50	113	193	312	516	659	755	834
1.0	0	0	0	0	1	2	5	14	29	56	126	215	347	576	737	845	935
1.3	0	0	0	0	1	2	5	16	33	63	140	238	384	637	818	939	1040
1.7	0	0	0	0	1	3	6	19	38	72	158	268	432	717	922	1060	1180
2.0	0	0	0	0	1	3	7	21	42	80	172	290	466	774	997	1150	1280
2.3	0	0	0	1	1	3	8	24	47	87	186	315	501	831	1070	1240	1380
2.7	0	0	0	1	1	3	9	27	53	98	206	343	547	907	1170	1360	1520
3.0	0	0	0	1	2	4	10	30	58	106	220	367	582	964	1250	1450	1620
3.3	0	0	0	1	2	4	11	32	63	113	234	388	615	1020	1320	1540	1720

Table 7. Flux emissivity correction quantity for water vapor-carbon dioxide overlap at -40C. Multiply values in table by 10^{-4} (Staley and Jurica, 1970).

log u_{CO_2}	log u_{H_2O}																
	−3.7	−3.3	−3.0	−2.7	−2.3	−2.0	−1.7	−1.3	−1.0	−0.7	−0.3	0.0	0.3	0.7	1.0	1.3	1.7
−4.0	0	0	0	0	0	0	0	0	1	1	2	3	5	8	9	10	11
−3.7	0	0	0	0	0	0	0	0	1	1	3	5	7	11	13	15	16
−3.3	0	0	0	0	0	0	0	1	1	2	4	7	11	17	20	23	24
−3.0	0	0	0	0	0	0	0	1	2	3	6	10	14	22	27	30	33
−2.7	0	0	0	0	0	0	0	1	2	4	8	13	19	29	36	40	43
−2.3	0	0	0	0	0	0	1	2	3	6	12	18	28	43	53	59	63
−2.0	0	0	0	0	0	0	1	2	4	8	16	25	37	58	71	79	85
−1.7	0	0	0	0	0	0	1	3	6	11	22	34	52	81	99	110	119
−1.3	0	0	0	0	0	1	2	5	10	18	35	56	84	130	160	178	192
−1.0	0	0	0	0	0	1	3	8	15	26	51	81	122	189	233	260	280
−0.7	0	0	0	0	1	2	4	11	21	37	72	114	172	267	329	368	398
−0.3	0	0	0	0	1	3	6	17	32	55	107	168	253	392	484	543	588
0.0	0	0	0	0	1	3	8	22	40	69	133	209	316	489	605	680	737
0.3	0	0	0	0	2	4	10	26	48	83	159	250	377	584	723	815	885
0.7	0	0	0	0	2	5	13	33	59	101	193	302	455	706	877	990	1080
1.0	0	0	0	0	3	7	15	38	68	114	217	340	511	794	988	1120	1210
1.3	0	0	0	1	3	8	18	44	77	128	243	380	571	886	1100	1250	1360
1.7	0	0	0	1	4	10	22	52	90	149	278	434	650	1010	1260	1420	1540
2.0	0	0	0	1	5	12	26	59	100	164	306	474	709	1100	1370	1550	1680
2.3	0	0	0	1	6	15	30	66	111	181	333	515	767	1190	1480	1680	1830
2.7	0	0	0	1	7	17	35	76	125	202	369	568	844	1300	1630	1850	2010
3.0	0	0	1	1	8	20	39	83	135	217	395	605	898	1390	1740	1980	2141
3.3	0	0	1	2	9	21	42	89	145	231	418	639	948	1460	1840	2090	2260

Table 8. Flux emissivity correction quantity for water vapor-carbon dioxide overlap at -10C. Multiply values in table by 10^{-4} (Staley and Jurica, 1970).

log u_{CO_2}	log u_{H_2O}																
	−3.7	−3.0	−3.0	−2.7	−2.3	−2.0	−1.7	−1.3	−1.0	−0.7	−0.3	0.0	0.3	0.7	1.0	1.3	1.7
−4.0	0	0	0	0	0	0	0	1	1	2	3	4	6	9	10	11	11
−3.7	0	0	0	0	0	0	0	1	2	2	4	6	9	13	15	16	16
−3.3	0	0	0	0	0	0	1	2	2	4	7	10	14	19	23	25	26
−3.0	0	0	0	0	0	0	1	2	3	5	9	13	18	26	31	33	34
−2.7	0	0	0	0	0	1	1	3	4	7	12	17	24	35	41	44	46
−2.3	0	0	0	0	0	1	2	4	7	10	17	25	36	51	60	65	68
−2.0	0	0	0	0	0	1	3	6	9	14	23	34	48	69	81	87	91
−1.7	0	0	0	0	1	2	4	8	12	19	33	48	67	96	113	122	128
−1.3	0	0	0	0	1	3	6	13	20	31	53	78	109	156	183	199	208
−1.0	0	0	0	0	2	4	9	19	30	46	78	114	160	227	267	290	304
−0.7	0	0	0	0	3	6	13	27	42	65	110	161	226	322	380	413	432
−0.3	0	0	0	1	4	10	19	40	63	96	164	239	335	478	564	614	643
0.0	0	0	0	1	5	13	25	50	79	121	206	300	421	600	709	773	810
0.3	0	0	0	1	7	16	30	61	96	146	248	360	505	722	854	932	978
0.7	0	0	1	2	9	20	38	75	117	179	303	440	617	882	1050	1140	1200
1.0	0	0	1	3	11	24	43	86	133	203	343	498	697	998	1180	1300	1360
1.3	0	0	1	3	13	28	50	97	150	228	385	555	781	1120	1330	1460	1520
1.7	0	0	1	4	16	33	59	113	174	262	441	637	890	1270	1520	1660	1740
2.0	0	0	2	5	19	38	66	125	191	288	483	696	971	1390	1650	1820	1900
2.3	0	0	2	6	22	43	73	137	209	314	525	754	1050	1500	1790	1960	2050
2.7	0	1	3	8	26	49	82	152	231	346	577	827	1150	1640	1960	2160	2250
3.0	0	1	3	9	28	53	89	163	246	368	612	876	1220	1740	2080	2290	2390
3.3	0	1	3	10	31	57	95	173	260	388	644	922	1280	1830	2190	2410	2520

Table 9. Flux emissivity correction quantity for water vapor-carbon dioxide overlap at 20C. Multiply values in table by 10^{-4} (Staley and Jurica, 1970).

log u_{CO_2}	log u_{H_2O}																
	−3.7	−3.3	−3.0	−2.7	−2.3	−2.0	−1.7	−1.3	−1.0	−0.7	−0.3	0.0	0.3	0.7	1.0	1.3	1.7
−4.0	0	0	0	0	0	0	1	1	2	2	4	5	7	9	10	11	11
−3.7	0	0	0	0	0	0	1	2	2	3	5	8	10	13	15	16	16
−3.3	0	0	0	0	0	1	1	2	4	5	8	12	16	21	23	24	25
−3.0	0	0	0	0	0	1	2	3	5	7	11	16	21	28	31	33	34
−2.7	0	0	0	0	1	1	2	4	7	9	15	21	28	37	42	44	45
−2.3	0	0	0	0	1	2	4	7	10	14	23	31	42	55	62	66	67
−2.0	0	0	0	0	1	3	5	9	13	19	31	42	56	75	84	89	91
−1.7	0	0	0	1	2	4	7	13	18	27	43	59	79	104	118	124	127
−1.3	0	0	0	1	3	7	11	20	30	44	70	96	128	170	192	202	207
−1.0	0	0	0	1	5	10	17	30	44	64	102	141	187	248	281	296	303
−0.7	0	0	1	2	7	14	24	43	63	91	145	201	266	354	400	423	432
−0.3	0	0	1	3	11	21	36	64	94	136	217	299	397	528	598	633	647
0.0	0	0	1	5	14	27	46	81	119	172	274	378	502	668	758	803	821
0.3	0	0	2	6	18	33	56	99	145	209	332	458	608	810	926	975	997
0.7	0	1	3	8	23	42	69	122	180	259	410	564	748	998	1140	1200	1230
1.0	0	1	3	10	27	49	79	140	205	295	467	641	849	1130	1290	1370	1400
1.3	0	1	4	12	32	55	90	158	231	332	524	719	952	1270	1450	1540	1580
1.7	0	2	5	15	38	65	104	181	266	381	600	820	1080	1450	1660	1760	1800
2.0	0	2	7	17	42	72	115	199	291	417	654	893	1180	1580	1800	1920	1970
2.3	0	3	8	19	47	79	125	216	315	451	706	962	1270	1700	1940	2070	2120
2.7	0	3	9	22	53	88	138	237	345	493	770	1050	1380	1850	2120	2270	2320
3.0	0	4	10	24	57	94	147	251	365	521	813	1110	1460	1950	2240	2400	2460
3.3	1	4	12	27	61	100	155	265	385	549	855	1160	1530	2050	2360	2520	2590

Table 10. Empirical constants used in Eqs. (15) and (16) (Roach, 1961).

Band λ (μ) Gas H_2O	c	k	C	D	K	A_c	I_0	Lower limit of validity pm gm cm^{-2} mb	A cm^{-1}
0·94	38	0·27	(− 135)	(230)	(125)	(200)	72·5	28	54
1·1	(42)	0·26	(− 292)	(345)	(180)	(300)	72·0	0·66	12
1·38	163	0·30	(251)	460	198	350	64·3	0·17	73
1·87	152	0·30	(143)	232	144	275	46·7	0·06	34
2·7	316	0·32	(316)	246	150	200	27·8	0·011	37
3·2	40·2	0·30	(− 144)	295	151	250	21·0	0·011	1
6·3	356	0·30	302	218	157	160	7·0	0·04	66
CO_2								cm atm mb	
1·4	0 058	0·41	-	-	-	80	63·7	$1·9 \times 10^3$	20
1·6	0·063	0·38	-	-	-	80	57·1	$1·9 \times 10^3$	12
2·0	0·192	0·39	(− 548)	138	114	80	43·2	$1·6 \times 10^4$	42
2·7	3·15	0·43	(− 137)	77	68	50	27·8	8·1	23
4·3	-	-	27·5	34	31·5	50	13·2	13·5	68
4·8	0·12	0·37	-	-	-	60	11·1	270	1
5·2	0·024	0·40	-	-	-	30	9·6	$2·5 \times 10^4$	2

Table 11. The function $\eta(\varphi)$ used in Eq. (17) for calculating absorption by the 9.6 μ band of ozone (Walshaw, 1957).

$\log_{10} \varphi$	$\eta(\varphi)$	$\log_{10} \varphi$	$\eta(\varphi)$
$\leq$ -4.0	1	-3.0	0.977
-3.9	0.998	-2.9	0.979
-3.8	0.995	-2.8	0.982
-3.7	0.993	-2.7	0.989
-3.6	0.989	-2.6	1.002
-3.5	0.984	-2.5	1.016
-3.4	0.982	-2.4	1.030
-3.3	0.980	-2.3	1.045
-3.2	0.977	-2.2	1.057
-3.1	0.977	-2.1	1.069
		-2.0	1.079

Table 12. Transmission, T, reflection, R, and absorption, A, values for low clouds as a function of solar zenith angle, ψ, to use in this research for the I_a^o component of the solar radiation.

ψ =	0°	10°	20°	30°	40°	50°	60°	70°	80°	90°
					LOW CLOUDS - STRATIFORM					
T	.39	.39	.38	.37	.34	.30	.25	.20	.18	.00
R	.56	.56	.57	.59	.62	.66	.72	.78	.80	1.0
A	.05	.05	.05	.04	.04	.04	.03	.02	.02	.00
					LOW CLOUDS - CUMULIFORM - UNDEVELOPED					
T	.50	.49	.48	.47	.45	.40	.32	.28	.25	.00
R	.46	.47	.48	.49	.52	.57	.65	.70	.73	1.0
A	.04	.04	.04	.04	.03	.03	.02	.02	.02	.00
					LOW CLOUDS - CUMULIFORM - DEVELOPED					
T	.12	.12	.12	.11	.10	.09	.08	.07	.05	.00
R	.78	.78	.78	.79	.81	.83	.86	.88	.92	1.0
A	.10	.10	.10	.10	.09	.08	.06	.05	.03	.00

Table 13. Transmission, T, reflection, R, and absorption, A, values for middle clouds as a function of solar zenith angle, ψ, to use in this research for the I_a^o component of the solar radiation.

ψ =	0°	10°	20°	30°	40°	50°	60°	70°	80°	90°
MIDDLE CLOUDS - AC,AS										
T	.64	.64	.64	.63	.59	.54	.47	.40	.33	.00
R	.32	.32	.32	.33	.38	.43	.51	.58	.65	1.0
A	.04	.04	.04	.04	.03	.03	.02	.02	.02	.00
MIDDLE CLOUDS - NS										
T	.20	.20	.20	.20	.19	.17	.13	.10	.10	.00
R	.66	.66	.66	.67	.69	.72	.78	.83	.85	1.0
A	.14	.14	.14	.13	.12	.11	.09	.07	.05	.00

Table 14. Transmission, T, reflection, R, and absorption, A, values for high clouds as a function of solar zenith angle, ψ, used in this research for the I_a^o component of the solar radiation.

ψ =	0°	10°	20°	30°	40°	50°	60°	70°	80°	90°
					HIGH CLOUDS					
T	.87	.86	.86	.85	.83	.80	.75	.66	.44	.00
R	.13	.14	.14	.15	.17	.20	.25	.34	.56	1.0
A	.00	.00	.00	.00	.00	.00	.00	.00	.00	.00

Table 15. Significant weather events during AMTEX '74 (Lenschow and Agee, 1974).

	Feb 1974	Major Synoptic Features
WARM PERIOD	14	Anticyclone Over East China Sea and Yellow Sea
	15	Cyclone Over Yellow Sea
	16	Anticyclone Over East China Sea and Yellow Sea
	17	Cyclone Over East China Sea
	18	Anticyclone Over East China Sea and Yellow Sea
	19	Cyclone Over East China Sea and Yellow Sea
	20	Cold Front Passage at Naha
	21	Anticyclone Over East China Sea and Yellow Sea
	22	Cyclong Over Yellow Sea and Sea of Japan (1004 mb)
	23	Cold Front Passage at Naha (FROPA)
COLD PERIOD	24	Cold Air Outbreak
	25	Cold Air Outbreak
	26	Cold Air Outbreak
	27	Cold Air Outbreak
	28	Cold Air Outbreak Weakens

Table 16. Spacially averaged cloud estimates for the AMTEX region on 18, 23, and 26 February 1974. The cloud fields in Figures 5-8 have been averaged to produce these values.

	Total Cloud Amount (Percent)	Low Cloud Amount (Percent)	Middle Cloud Amount (Percent)	High Cloud Amount (Percent)
18 Feb	33	24	19	8
23 Feb	77	55	58	18
26 Feb	87	72	68	30

Table 17. Clear sky and cloud contributions to the radiative budget components at Naha on February 23, 1974, 0900 JST. Terms are defined as in Table 15. Computed values (in mW cm^{-2}) were obtained assuming a completely clear or overcast condition of the cloud layers. Values are positive in the direction of the arrows.

		$rad\downarrow_{100}$	$rad\uparrow_{100}$	$rad\uparrow\downarrow_{100}$	$rad\downarrow_{sfc}$	$rad\uparrow_{sfc}$	$rad\uparrow\downarrow_{sfc}$	$rad]^{100}_{sfc}$	Cool Rate °C/day
Clear	LW	2.0	25.2	23.2↑	32.5	41.9	9.4↑	13.8	1.286
	SW	32.3	5.9	26.4↓	24.7	3.5	21.2↓	-5.2	-.492
	NET	34.3	31.1	3.2↓	57.2	45.4	11.8↓	8.6	0.794
Sc	LW	2.0	24.4	22.4↑	41.7	41.9	0.2↑	22.2	2.061
	SW	32.3	19.5	12.8↓	8.2	1.2	7.0↓	-5.8	-.545
	NET	34.3	43.9	9.6↓	49.9	43.1	6.8↓	16.4	1.516
Ac	LW	2.0	21.2	19.2↑	39.7	41.9	2.2↑	17.0	1.574
	SW	32.3	17.2	15.1↓	12.8	1.8	11.0↓	-4.1	-.384
	NET	34.3	38.4	4.1↑	52.5	43.7	8.8↓	12.9	1.190
Ci	LW	2.0	14.6	12.6↑	36.9	41.9	5.0↑	7.6	0.706
	SW	32.3	11.3	21.0↓	19.4	2.8	16.6↓	-4.4	-.418
	NET	34.3	25.9	8.4↓	56.3	44.7	11.6↓	3.2	0.288
Sc and Ac	LW	2.0	21.2	19.2↑	41.7	41.9	0.2↑	19.0	1.764
	SW	32.3	24.3	8.0↓	7.4	1.0	6.4↓	-1.7	-.164
	NET	34.3	45.5	11.2↑	49.1	42.9	6.2↓	17.3	1.600
Sc and Ci	LW	2.0	14.6	12.6↑	41.7	41.9	0.2↑	12.4	1.157
	SW	32.3	23.1	9.2↓	8.7	1.2	7.5↓	-1.7	-.161
	NET	34.3	37.7	3.4↑	50.4	43.1	7.3↓	10.7	0.996
Ac and Ci	LW	2.0	14.6	12.6↑	39.7	41.9	2.2↑	10.4	0.967
	SW	32.3	19.4	12.9↓	13.0	1.7	11.3↓	-1.6	-.153
	NET	34.3	34.0	0.3↓	52.7	43.6	9.1↓	8.8	0.814
Sc, Ac, and Ci	LW	2.0	14.6	12.6↑	41.7	41.9	0.2↑	12.4	1.157
	SW	32.3	24.6	7.7↓	7.1	0.9	6.2↓	-1.5	-.152
	NET	34.3	39.2	4.9↑	48.8	42.8	6.0↓	10.9	1.005

Table 18. The longwave (LW) and shortwave (SW) radiation budget of the troposphere, $rad\uparrow_{100}$, $rad\downarrow_{100}$, and $rad\uparrow\downarrow_{100}$ refer to the upward directed radiation at 100 mb, the downward directed radiation at 100 mb, and the net radiation at 100 mb, rexpectively. $rad\uparrow_{sfc}$, $rad\downarrow_{sfc}$, and $rad\uparrow\downarrow_{sfc}$ are the corresponding values at the surface and $rad]^{100}_{sfc}$ is the radiative flux divergence in the layer surface to 100 mb. Units are in mW cm^{-2}.

		$rad\downarrow_{100}$	$rad\uparrow_{100}$	$rad\uparrow\downarrow_{100}$	$rad\downarrow_{sfc}$	$rad\uparrow_{sfc}$	$rad\uparrow\downarrow_{sfc}$	$rad]^{100}_{sfc}$	Cool Rate °C/day	Net Cool Rate
18 Feb 74	LW	2.0	24.4	22.4↑	34.7	42.3	7.7↑	14.7	1.358	
										0.941
	SW	31.5	11.5	20.0↓	18.1	2.6	15.5↓	-4.4	-0.417	
23 Feb 74	LW	2.0	21.4	19.4↑	38.2	42.7	4.5↑	14.9	1.376	
										0.981
	SW	32.4	18.3	16.1↓	11.8	1.7	10.1↓	-4.2	-0.395	
26 Feb 74	LW	2.0	19.9	17.9↑	35.9	42.2	6.4↑	11.5	1.055	
										0.711
	SW	33.4	19.6	13.8↓	11.8	1.7	10.1↓	-3.7	-0.343	

Table A-1. Table of bases and tops of the 15 layers of the 3DNEPH cloud analysis.

LAYER	BASE OF LAYER (ft.)	TOP OF LAYER (ft.)
1	SFC	150 AGL
2	151	300 AGL
3	301	600 AGL
4	601	1000 AGL
5	1001	2000 AGL
6	2001	3500 AGL
7	3501	5000 MSL
8	5001	6500 MSL
9	6501	10000 MSL
10	10001	14000 MSL
11	14001	18000 MSL
12	18001	22000 MSL
13	22001	26000 MSL
14	26001	35000 MSL
15	35001	55000 MSL

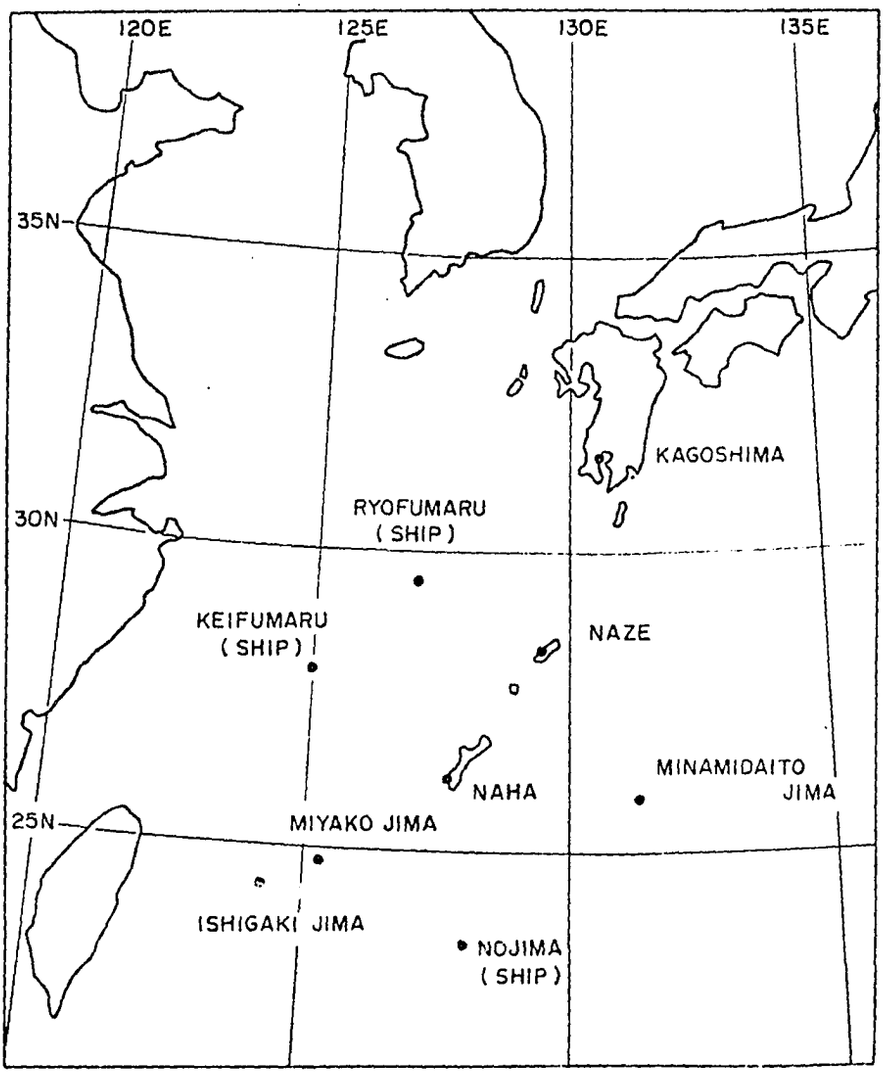

Fig. 1. Geographic region around the Southwest Islands of Japan and station locations during AMTEX.

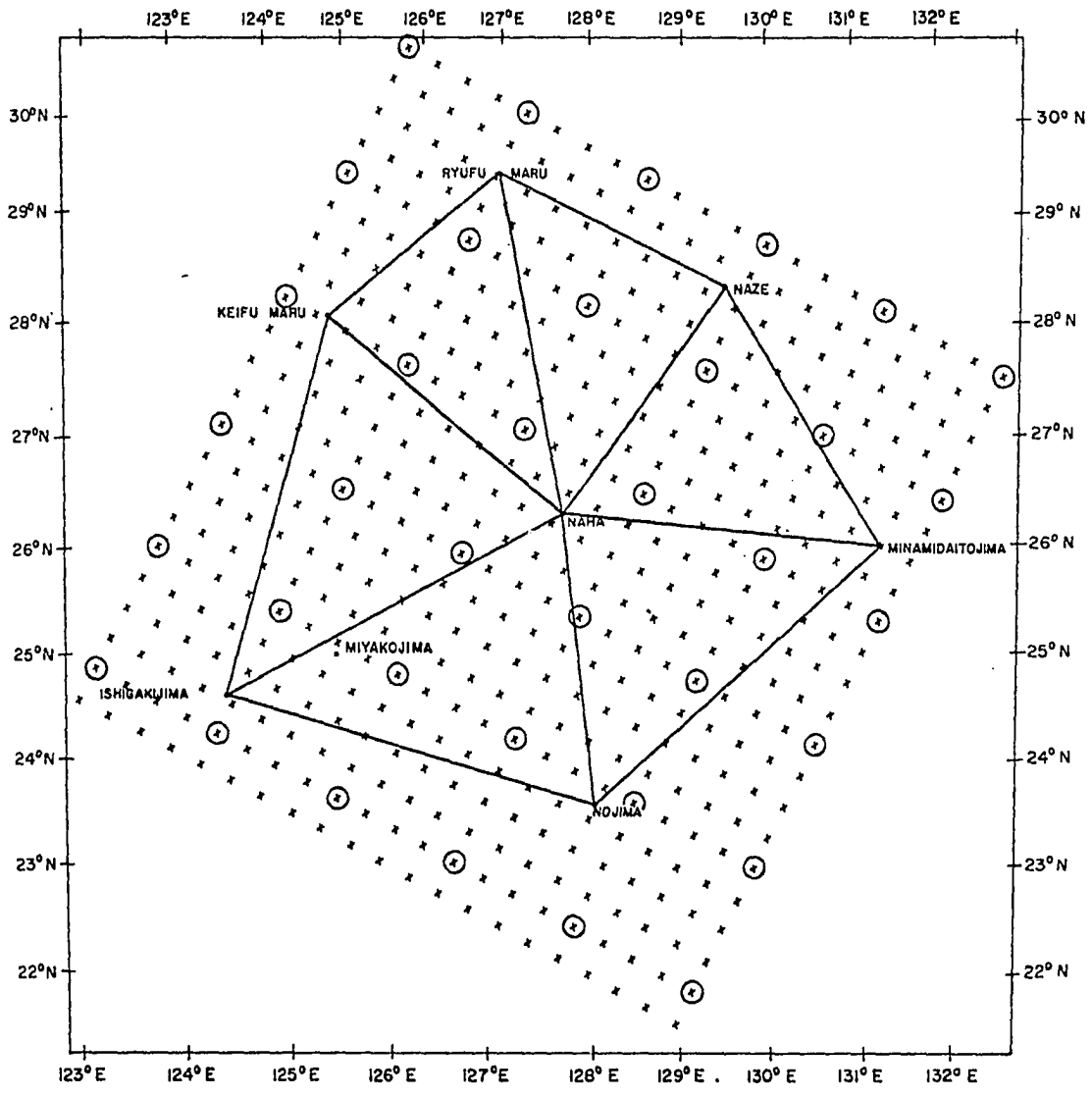

Fig. 2. Station locations during AMTEX, and grid squares for which cloud information from the 3DNEPH is available. The circled grid points represent the 6 by 6 grid field established for this study.

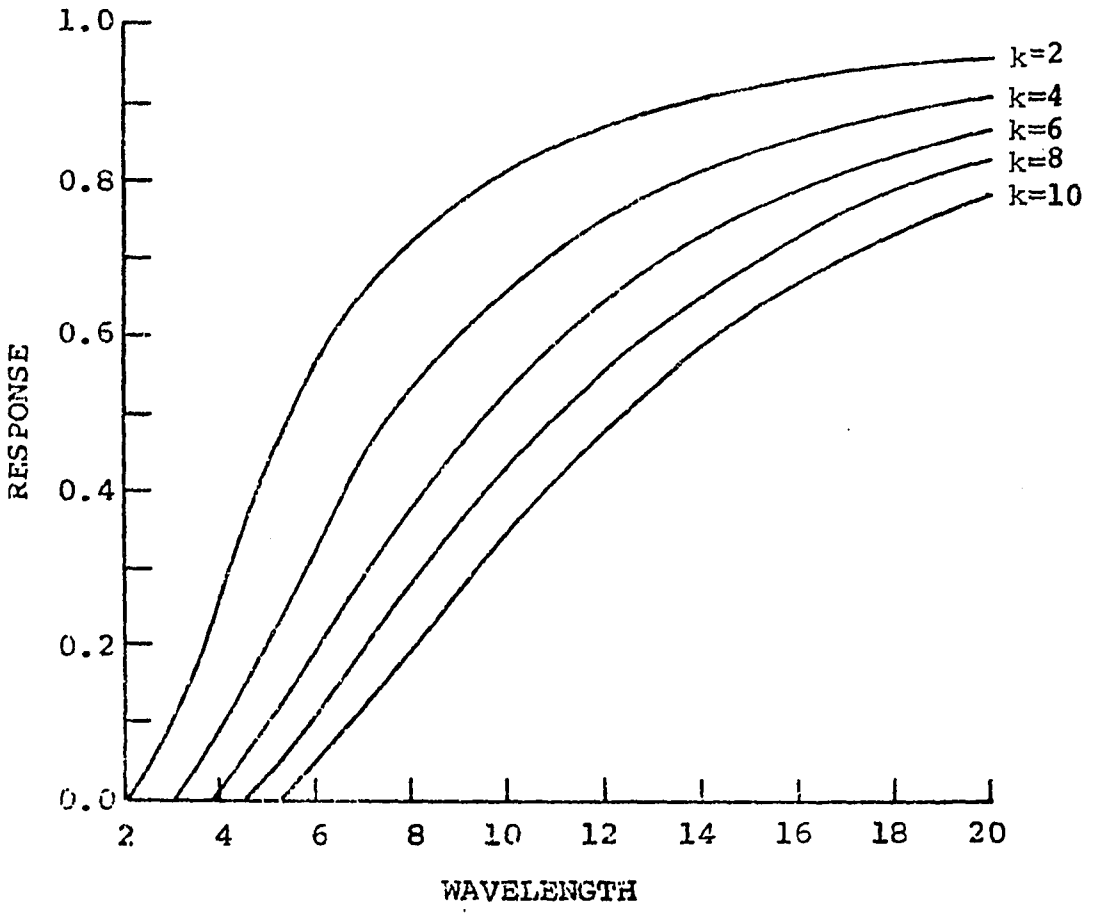

Fig. 3. Response function for the exponential weighting function in Eq. (2) for varying values of k. Wavelength is expressed in grid intervals.

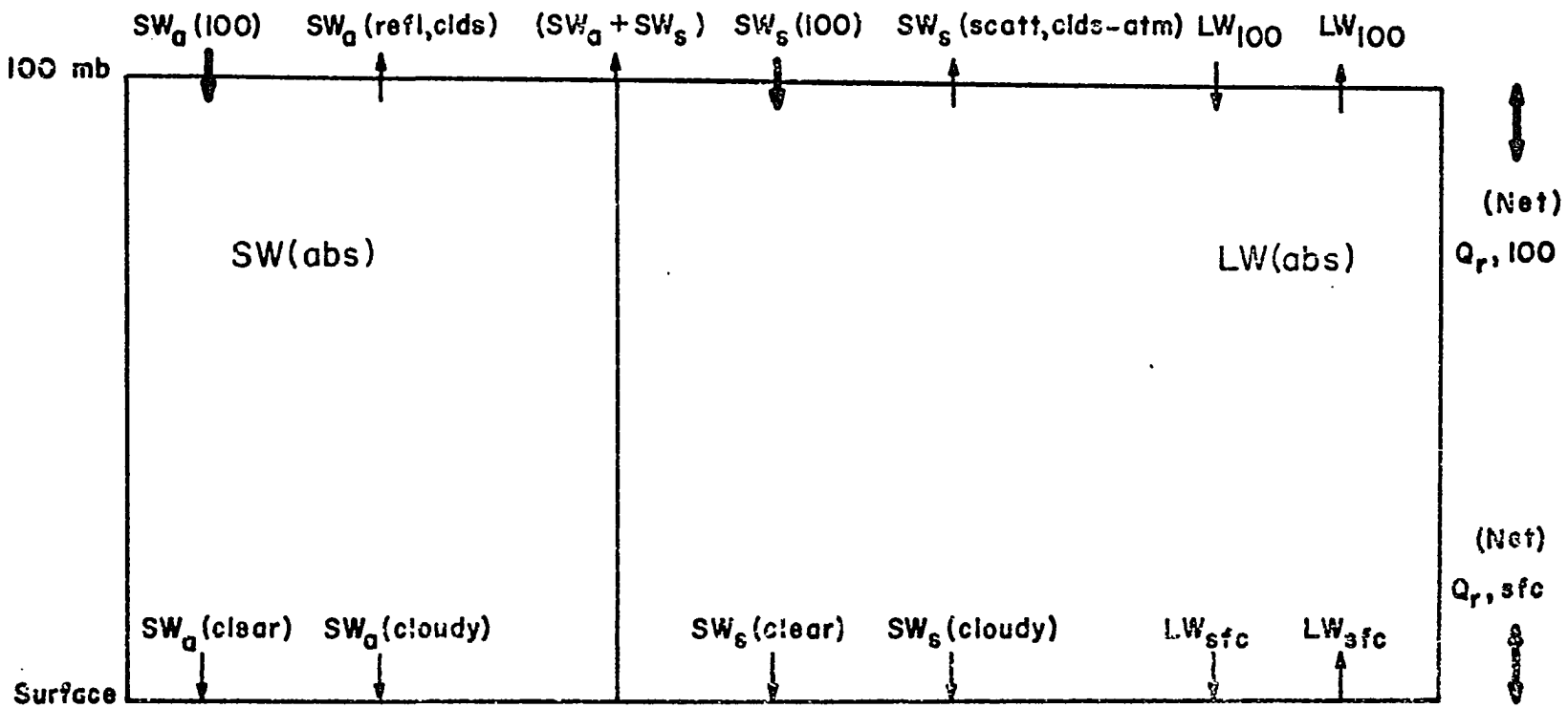

Fig. 4. Schematic representation of the radiation budgets of the atmospheric column from 100 mb to the surface. The positive directions of solar (SW) and terrestrial (LW) irradiances are represented by arrowheads. Refl, scatt, and abs refer to reflected, scattered and absorbed, respectively. The subscripts a and s indicate the absorbed and scattered components of the solar radiation (See Eqs. (34) and (35)).

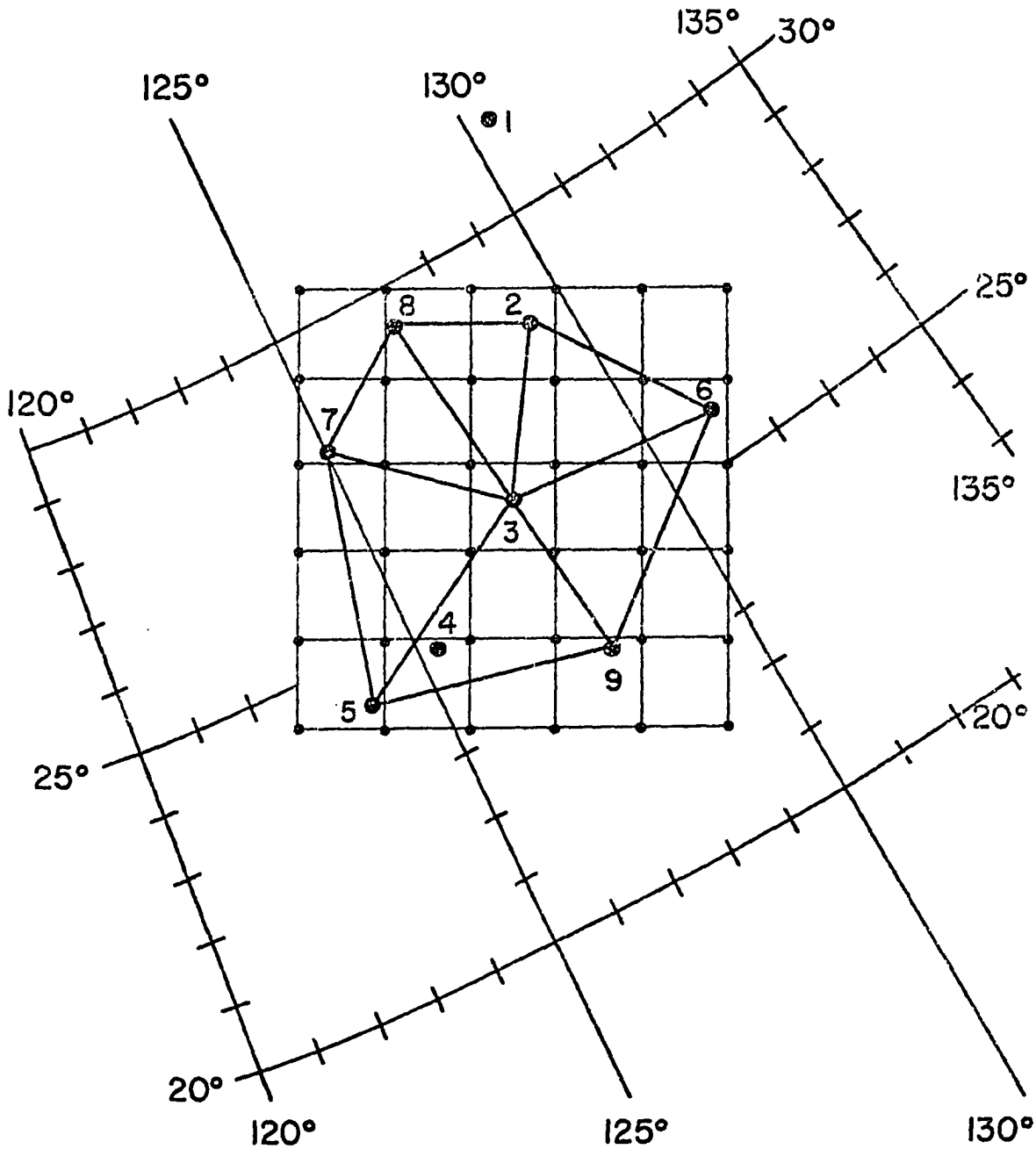

Fig. 5. The 6 by 6 grid field established for this study. The Japan Meteorological Agency stations used in the study are indicated by the following numbers: 1. Kagoshima, 2. Naze, 3. Naha, 4. Miyakojima, 5. Ishigakijima, 6. Minamidaitojima, 7. Keifu Maru, 8. Ryofu Maru, and 9. Nojima.

0	14	16	49	15	0	64	77	90	85	80	70
17	25	31	32	5	61	90	85	96	85	44	70
16	10	34	39	20	59	98	93	100	78	64	66
14	10	32	48	41	31	96	100	84	43	56	64
37	52	53	52	67	6	91	94	72	67	64	73
59	71	66	58	25	6	96	81	62	43	59	60

18 FEB 1974 23 FEB 1974

53	86	80	94	76	90
66	77	66	90	78	99
79	64	85	78	96	99
82	73	99	96	91	96
89	94	87	100	100	100
97	94	99	100	100	73

26 FEB 1974

Fig. 6. Mean daily total cloud cover, in percent, at the grid points used for this study (Ref. Fig. 5).

0	11	16	38	11	0
9	25	31	32	5	50
16	6	22	26	15	55
1	4	12	18	18	31
21	36	62	15	32	6
34	55	68	56	25	0

18 FEB 1974

21	63	74	82	79	52
86	65	71	63	34	41
95	85	54	48	40	41
83	95	59	20	37	20
85	84	67	41	55	41
65	77	0	17	16	35

23 FEB 1974

53	67	77	88	68	86
66	65	60	83	64	74
77	64	61	55	82	74
67	70	82	78	45	88
59	63	84	100	100	55
62	57	85	84	100	48

26 FEB 1974

Fig. 7. Mean daily low cloud cover, in percent, at the grid points used for this study (Ref. Fig. 5).

0	4	10	38	9	0	55	31	78	73	68	61
12	0	0	0	4	45	76	32	63	78	28	55
0	7	19	17	7	45	66	63	99	61	37	46
0	8	26	36	19	19	72	64	61	39	49	63
17	41	44	46	56	0	49	62	46	41	51	72
54	49	21	14	25	1	78	55	62	38	49	51

18 FEB 1974 23 FEB 1974

0	74	75	91	75	25
43	50	47	87	74	92
52	0	79	76	75	92
27	46	68	85	89	69
56	85	82	94	82	99
88	84	91	83	77	49

26 FEB 1974

Fig. 8. Mean Daily middle cloud cover, in percent, at the grid points used for this study (Ref. Fig. 5).

0	C	10	15	0	0	16	25	25	6	0	19
0	0	0	0	4	37	45	20	16	6	31	25
0	0	0	0	0	33	50	10	0	7	25	31
13	10	7	23	5	0	0	14	39	35	15	24
9	0	1	35	45	0	25	15	13	40	15	16
9	1	24	0	0	5	25	13	C	0	0	0

18 FEB 1974 23 FEB 1974

C	58	68	40	0	0
15	36	25	36	52	99
17	0	C	0	0	99
11	22	50	67	C	0
64	93	0	0	0	0
72	94	25	25	0	0

26 FEB 1974

Fig. 9. Mean daily high cloud cover, in percent, at the grid points used for this study (Ref. Fig. 5).

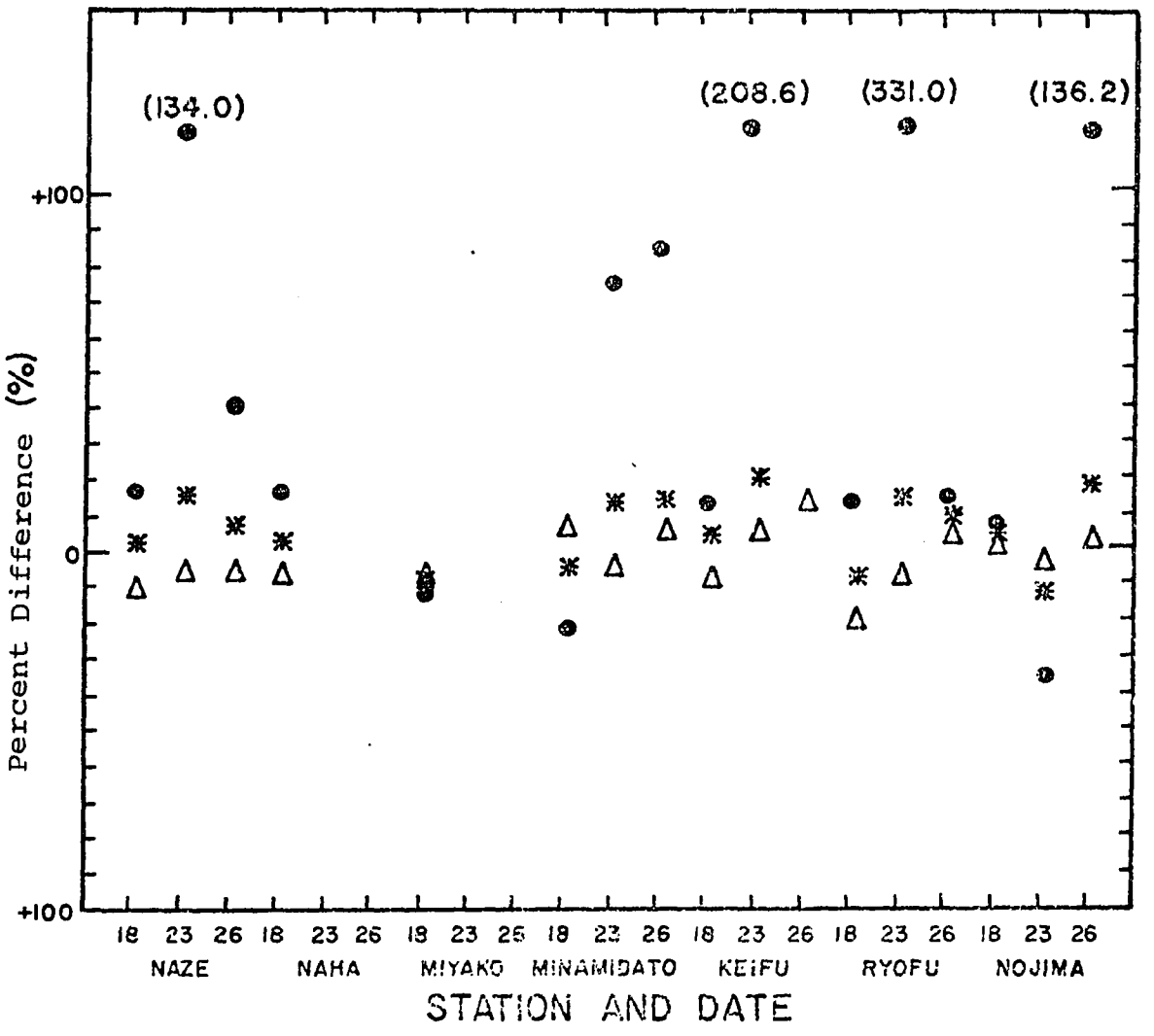

Fig. 10. Percent difference between the calculated and observed long wave (Δ), short wave (·), and total (*) downward fluxes at the surface on February 18, 23, and 26, 1974, at the stations for which measurements were made.

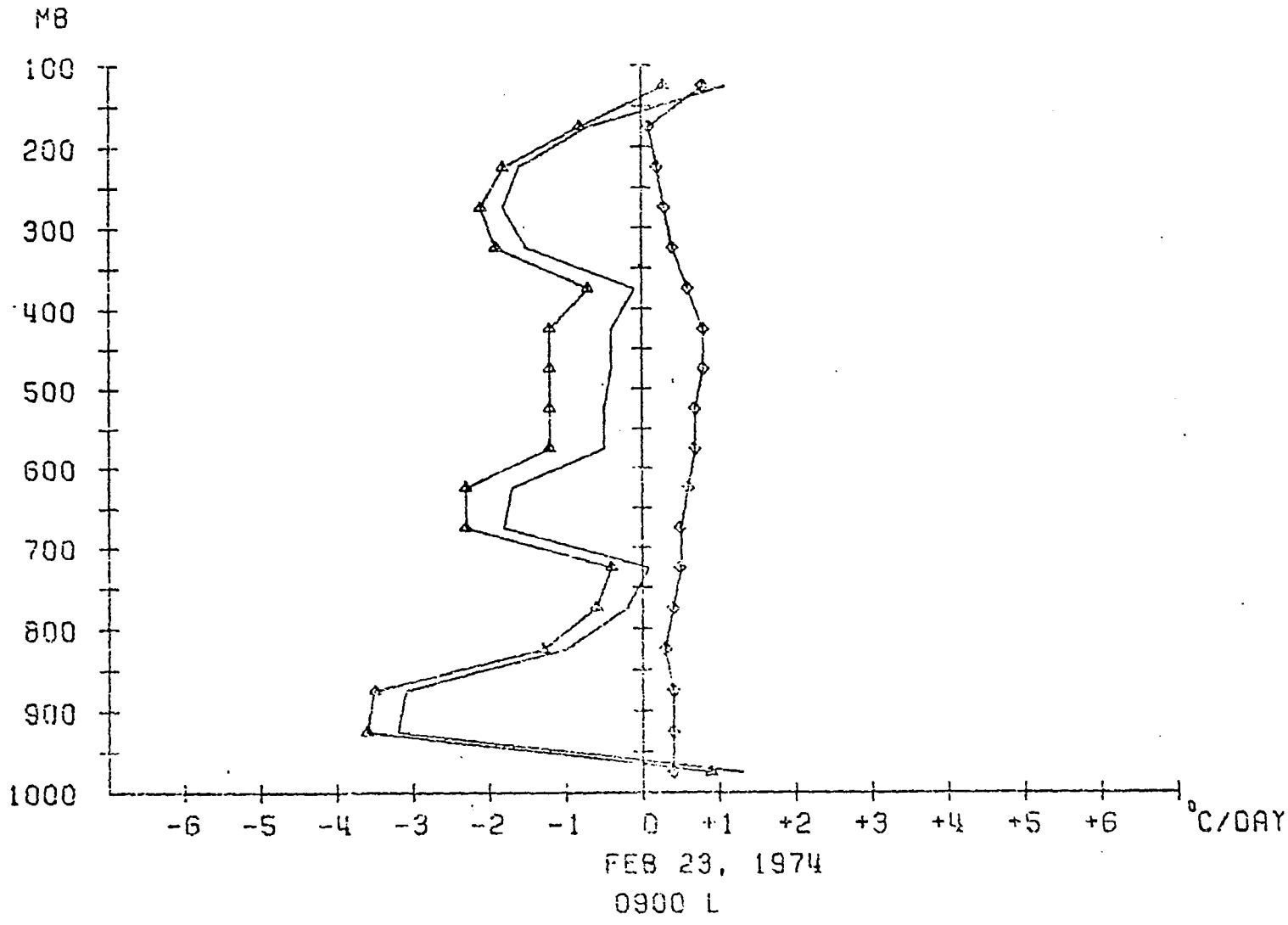

Fig. 11. Vertical profiles of terrestrial cooling (Δ), solar heating (◊), and the net radiational cooling (solid line) for a grid point in AMTEX on February 23, 1974.

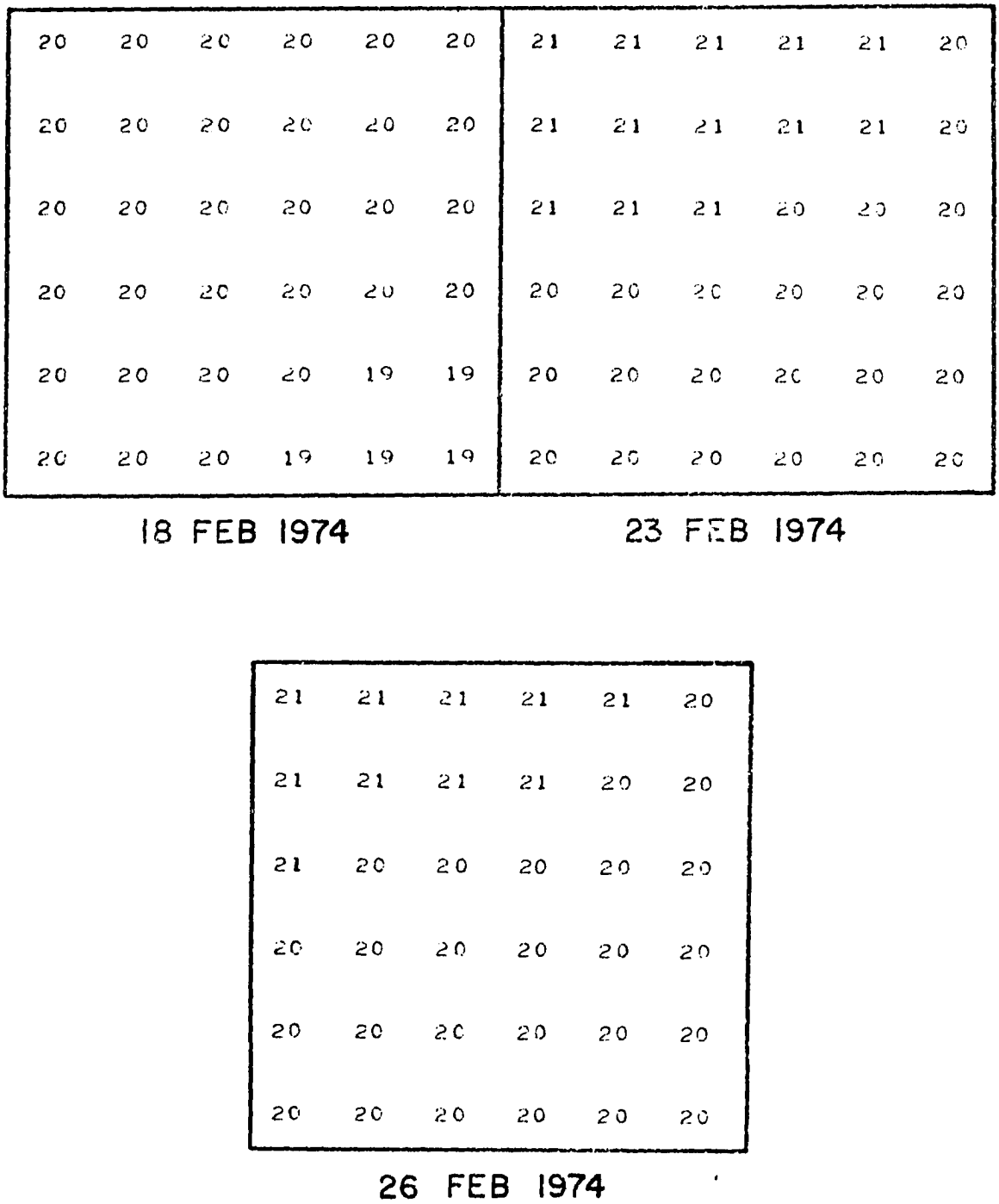

Fig. 12. Downward long wave fluxes at 100 mb, ($LW\downarrow_{100}$) x 10 mW/cm^2, at the grid points used for this study (Ref. Fig. 5).

259	256	251	239	257	260	222	211	199	203	221	212
250	256	255	254	258	218	191	217	212	209	220	209
254	258	252	252	261	219	186	221	201	216	215	212
249	249	240	213	240	251	227	199	209	224	216	202
243	237	240	206	204	261	214	201	219	223	227	202
230	231	216	247	255	255	214	212	225	244	232	240

18 FEB 1974 23 FEB 1974

233	172	178	186	221	222
207	198	212	189	190	150
197	224	216	218	204	150
210	213	185	180	210	228
181	155	220	211	214	221
164	155	193	201	222	227

26 FEB 1974

Fig. 13. Upward long wave fluxes at 100 mb, ($LW\uparrow_{100}$) x 10 mW/cm^2, at the grid points used for this study (Ref. Fig. 5).

239	236	231	219	238	240
230	235	235	234	238	198
234	238	232	232	241	199
229	230	220	194	220	231
223	218	220	186	185	242
210	211	197	227	236	236

18 FEB 1974

201	190	178	182	201	191
170	196	192	189	200	189
165	200	180	195	195	192
207	179	189	204	196	181
194	181	199	203	207	182
194	192	205	224	212	219

23 FEB 1974

212	151	157	165	200	201
187	177	192	169	170	130
177	203	195	198	184	130
190	193	165	159	189	208
161	135	200	191	194	201
144	135	173	181	203	207

26 FEB 1974

Fig. 14. Net long wave fluxes at 100 mb, $(LW\uparrow\downarrow_{100})$ x 10 mW/cm^2, at the grid points used for this study (Ref. Fig. 5). Positive values indicate net upward fluxes.

296	307	311	345	321	316
313	326	335	340	317	377
313	315	345	356	343	386
317	322	347	366	366	356
356	365	384	377	387	341
373	385	391	388	357	340

18 FEB 1974

352	367	394	403	396	379
370	367	396	394	361	383
374	378	399	390	377	383
386	399	387	359	377	374
395	403	389	378	385	389
402	394	365	362	376	381

23 FEB 1974

314	336	340	356	343	377
316	331	334	358	350	376
326	331	347	346	379	382
341	338	369	372	365	390
353	359	370	382	387	390
358	359	379	384	386	386

26 FEB 1974

Fig. 15. Downward long wave fluxes at the surface, $(LW\downarrow_{sfc})$ x 10 mW/cm^2, at the grid points used for this study (Ref. Fig. 5).

415	415	409	412	412	413
407	416	416	413	413	413
400	420	427	428	440	440
415	414	424	440	440	440
417	408	431	440	440	440
414	414	426	440	440	440

18 FEB 1974

420	420	419	419	419	416
408	420	420	419	416	425
395	403	418	437	437	437
414	416	420	442	444	444
427	428	441	444	444	444
428	431	443	444	444	444

23 FEB 1974

415	415	409	412	412	413
407	421	417	408	408	412
391	399	420	420	424	438
411	411	420	437	444	444
412	412	442	444	445	445
412	413	444	444	444	444

26 FEB 1974

Fig. 16. Upward long wave fluxes from the surface, ($LW\uparrow_{sfc}$) x 10 mW/cm^2, at the grid points used for this study (Ref. Fig. 5).

119	107	98	67	91	97	68	52	25	16	23	37
94	90	80	73	96	36	38	52	23	25	55	42
87	105	82	73	97	55	21	25	19	47	59	54
98	92	78	74	74	84	28	17	33	83	67	71
62	44	47	64	54	99	32	25	52	66	59	55
41	29	35	51	83	100	27	37	78	82	69	63

18 FEB 1974 23 FEB 1974

101	79	70	56	69	35
91	90	83	50	57	36
64	68	73	74	45	55
70	73	51	65	79	54
58	53	72	62	59	55
53	55	65	59	58	57

26 FEB 1974

Fig. 17. Net long wave fluxes at the surface, $(LW\uparrow\downarrow_{sfc})$ x 10 mW/cm^2, at the grid points used for this study (Ref. Fig. 5). Positive values indicate net downward fluxes.

100	102	103	104	105	107
103	104	105	106	108	109
105	106	107	109	110	111
108	109	110	111	112	113
110	111	113	113	114	115
112	113	114	115	116	117

18 FEB 1974

104	105	106	107	109	110
106	107	108	110	111	112
108	110	111	112	113	114
111	112	113	114	115	116
113	114	115	116	117	118
115	116	117	118	119	120

23 FEB 1974

107	109	110	111	112	113
110	111	112	113	114	115
112	113	114	115	117	117
114	115	116	117	118	119
116	117	118	119	120	121
118	119	120	121	122	123

26 FEB 1974

Fig. 18. The amount of short wave radiation subject to absorption that is input at 100 mb, $(SW_a{\downarrow}_{100})$ x 10 mW/cm^2, at the grid points used for this study (Ref. Fig. 5).

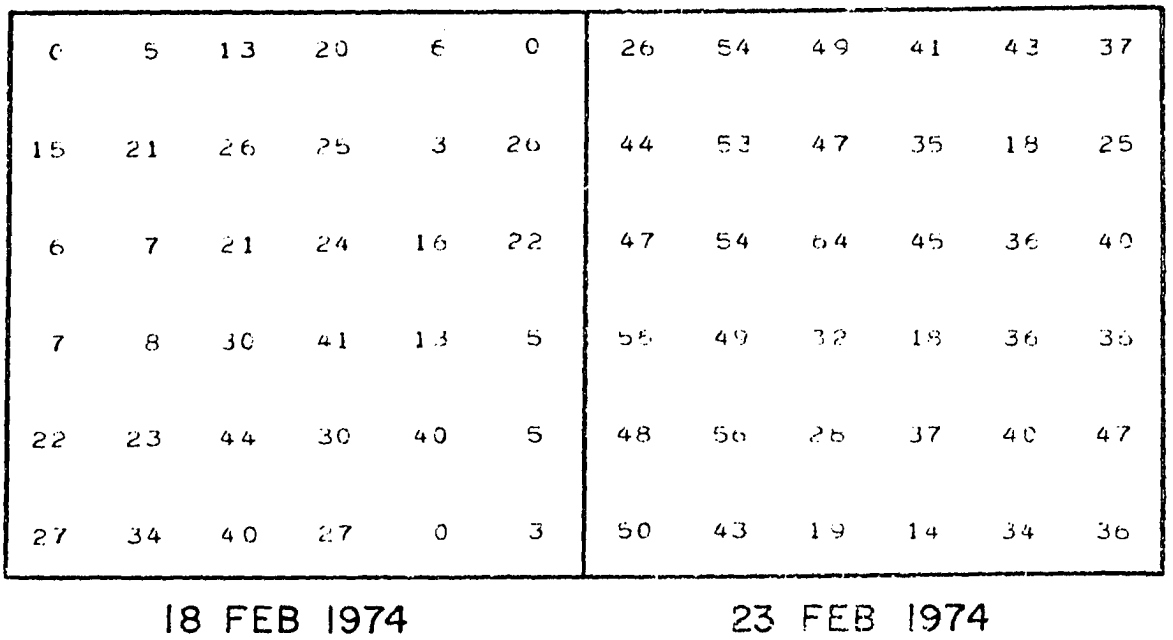

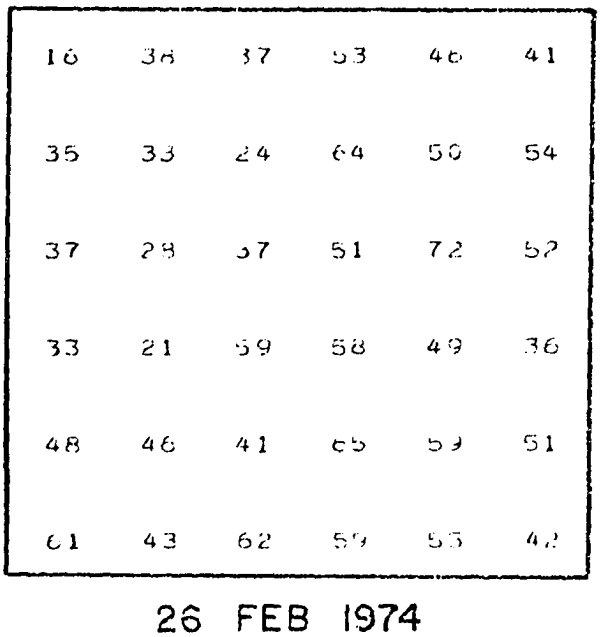

Fig. 19. The amount of short wave radiation subject to absorption that is reflected upward by the clouds, $(SW_a\uparrow_{100}$ (refl, clds)) x 10 mW/cm^2, at the grid points used for this study (Ref. Fig. 5).

0	2	7	15	5	0
9	8	9	13	3	20
2	5	14	15	8	16
11	8	19	29	11	2
14	16	16	24	33	2
20	21	38	14	0	5

18 FEB 1974

28	17	20	10	16	19
10	19	10	25	11	18
17	19	0	19	14	30
20	26	17	12	22	33
28	27	13	19	24	29
29	25	19	8	24	26

23 FEB 1974

6	26	24	9	19	16
20	17	12	20	24	30
19	11	21	11	27	29
12	17	33	33	36	29
10	24	15	33	30	28
12	36	23	25	36	17

26 FEB 1974

Fig. 20. The amount of the short wave radiation component subject to absorption that reaches the surface through clouds, $(SW_a{\downarrow}_{sfc}$ (clds)) x 10 mW/cm^2, at the grid points used for this study (Ref. Fig. 5).

59	53	44	30	50	59
38	29	22	23	55	23
50	48	28	25	37	31
43	47	22	7	37	54
27	26	15	20	7	53
22	11	4	18	61	54

18 FEB 1974

14	0	7	12	7	13
8	0	2	7	31	21
0	0	1	5	13	1
0	0	19	36	14	9
2	1	25	11	9	2
2	13	34	43	15	6

23 FEB 1974

46	16	17	8	12	5
22	22	36	4	13	0
16	28	15	5	0	2
21	36	0	1	0	5
15	9	18	0	1	0
4	9	1	0	1	8

26 FEB 1974

Fig. 21. The amount of the short wave radiation component subject to absorption that reaches the surface through clear sky, ($SW_a{\downarrow}_{sfc}$ (clear)) x 10 mW/cm^2, at the grid points used for this study (Ref. Fig. 5).

190	192	194	197	199	202
194	196	199	201	203	206
199	201	203	205	207	210
203	205	207	209	211	213
207	209	212	213	215	217
211	213	215	217	219	221

18 FEB 1974

196	198	200	203	205	208
200	203	205	207	209	212
205	207	209	211	213	215
209	211	213	215	217	219
213	215	218	219	220	222
217	219	220	222	224	226

23 FEB 1974

203	205	207	210	212	214
207	209	211	213	216	218
211	213	215	217	219	221
215	217	219	221	223	225
219	221	224	224	226	228
223	225	226	228	230	231

26 FEB 1974

Fig. 22. The amount of the short wave radiation component subject to scattering that is input at 100 mb, $(SW_s{\downarrow}_{100})$ x 10 mW/cm^2, at the grid points used for this study (Ref. Fig. 5).

23	36	52	80	42	24
59	81	95	94	32	84
40	44	80	88	70	79
36	41	89	118	60	39
80	86	124	91	123	40
92	118	144	111	25	31

18 FEB 1974

91	144	132	119	132	118
126	147	145	123	71	96
147	150	147	136	121	141
152	151	109	71	122	124
149	157	99	128	135	157
153	130	72	62	116	145

23 FEB 1974

64	114	114	135	129	137
110	105	80	153	129	157
118	97	118	139	169	154
110	74	154	150	138	155
112	141	126	170	165	159
141	139	168	168	168	141

26 FEB 1974

Fig. 23. The amount of the short wave radiation component subject to scattering that is scattered upward by clouds and atmosphere, ($SW_s\uparrow_{100}$ (scatt, clds - atm)) x 10 mW/cm^2, at the grid points used for this study (Ref. Fig. 5).

0	7	20	34	13	0	63	54	46	44	50	48
24	33	40	40	8	50	48	56	54	62	38	48
9	14	39	42	26	36	58	57	58	58	51	72
36	21	51	69	36	9	57	59	45	29	52	66
41	44	43	61	70	9	58	54	40	57	57	58
49	62	58	49	0	17	59	49	43	22	62	60

18 FEB 1974 23 FEB 1974

23	52	47	52	50	63
42	48	33	49	50	61
51	41	54	63	51	61
48	41	65	68	84	55
65	55	46	54	58	69
72	60	54	60	59	65

26 FEB 1974

Fig. 24. The amount of the short wave component subject to scattering that reaches the surface through clouds, $(SW_s{\downarrow}_{sfc}$ (clds)) x 10 mW/cm^2, at the grid points used for this study (Ref. Fig. 5).

167	148	122	82	144	178	41	0	22	39	24	41
111	82	64	67	164	71	26	0	6	22	100	68
149	143	84	74	111	95	0	0	4	17	41	3
129	143	67	22	115	166	0	0	58	115	43	29
85	80	45	61	22	169	6	4	78	34	28	8
70	33	13	58	194	172	5	39	105	138	46	20

18 FEB 1974 23 FEB 1974

117	40	46	23	33	14
56	56	98	11	36	0
42	76	43	15	0	7
57	102	0	3	0	15
43	25	52	0	3	0
11	26	4	0	3	25

26 FEB 1974

Fig. 25. The amount of the short wave radiation component subject to scattering that reaches the surface through clear sky, ($SW_{s\downarrow sfc}$ (clear)) x 10 mW/cm^2, at the grid points used for this study (Ref. Fig. 5).

32	30	27	23	30	34
26	22	20	20	33	23
30	30	24	22	26	25
32	31	23	18	29	33
24	24	17	24	18	34
23	18	15	20	37	36

18 FEB 1974

20	10	13	16	14	17
14	11	11	16	20	22
11	11	10	14	17	15
11	12	20	28	18	19
13	12	23	17	17	13
13	17	29	31	21	16

23 FEB 1974

27	18	19	14	16	14
19	20	25	12	17	12
18	22	19	14	10	14
20	28	13	14	17	14
20	16	19	11	12	14
15	18	11	12	13	17

26 FEB 1974

Fig. 26. The sum of the amounts of short wave radiation components subject to absorption and scattering that reaches the surface and is reflected, $((SW_a + SW_s)\uparrow)$ x 10 mW/cm^2, at the grid points used for this study (Ref. Fig. 5).

4	14	26	40	11	-10
33	60	72	67	-4	18
6	12	47	53	36	4
-6	-3	45	51	0	-17
33	30	81	5	38	-11
29	56	67	53	-36	-30

18 FEB 1974

39	95	65	48	76	46
48	97	81	46	-4	9
57	98	82	68	43	58
106	68	25	-7	41	25
78	78	16	51	61	59
77	49	-12	-9	40	71

23 FEB 1974

9	7	10	46	67	66
34	16	-1	71	36	20
27	25	40	70	99	11
23	-15	56	44	53	70
5	0	44	93	83	75
19	-9	68	71	87	53

26 FEB 1974

Fig. 27. Net upward irradiance (long and short wave) at 100 mb, $(Q_{r,100}^{(Net)} \uparrow) \times 10$ mW/cm^2, at the grid points used for this study (Ref. Fig. 5). Negative values represent net downward irradiance.

75	73	67	71	91	106
63	39	35	48	101	106
93	75	59	61	58	98
92	95	58	36	95	112
83	98	55	79	60	100
98	79	64	68	135	113

18 FEB 1974

58	9	57	74	60	67
40	12	38	74	99	90
43	40	33	39	42	37
39	58	86	82	44	47
49	49	82	37	42	28
55	71	95	99	58	33

23 FEB 1974

64	37	46	22	28	48
29	33	71	23	49	42
46	65	42	6	22	30
49	90	34	26	24	36
54	44	40	14	21	28
30	59	6	14	29	41

26 FEB 1974

Fig. 28. Net downward irradiance (long and short wave) at the surface, $(Q_{r,sfc}^{(Net)}\downarrow)$ x 10 mW/cm^2, at the grid points used for this study (Ref. Fig. 5).

-119	-127	-131	-150	-146	-142
-135	-144	-154	-160	-141	-162
-146	-132	-149	-159	-143	-143
-130	-137	-141	-119	-145	-146
-161	-173	-172	-122	-130	-142
-168	-181	-161	-175	-152	-135

18 FEB 1974

-132	-137	-152	-165	-177	-154
-131	-143	-167	-163	-144	-146
-143	-174	-160	-147	-135	-137
-178	-160	-155	-120	-128	-110
-161	-156	-146	-136	-147	-126
-166	-154	-126	-140	-142	-155

23 FEB 1974

-110	-71	-87	-108	-130	-165
-95	-86	-107	-118	-112	-93
-111	-134	-122	-123	-138	-73
-119	-119	-113	-93	-109	-153
-101	-81	-127	-128	-134	-144
-90	-79	-107	-121	-144	-149

26 FEB 1974

Fig. 29. Absorption of long wave radiation, $(-\text{rad}]_{\text{sfc}}^{100})$ x 10 mW/cm^2, at the grid points used for this study (Ref. Fig. 5). Negative values represent radiative flux divergence in the column from 100 mb to the surface.

41	42	39	39	44	48
41	47	47	45	46	39
47	46	44	45	49	42
47	46	39	33	51	53
47	46	37	39	34	55
42	47	31	55	54	54

18 FEB 1974

36	34	31	44	42	41
44	35	50	43	51	48
44	37	46	42	50	43
34	37	46	48	43	38
35	30	50	49	44	40
35	35	44	53	45	51

23 FEB 1974

39	28	31	41	36	51
33	39	39	26	28	32
40	46	41	48	18	33
48	41	24	25	33	49
43	38	45	22	31	42
41	31	34	37	29	56

26 FEB 1974

Fig. 30. Absorption of short wave radiation, $(-\text{rad}]_{\text{sfc}}^{100})$ x 10 mW/cm^2, at the grid points used for this study (Ref. Fig. 5).

1101	1179	1215	1389	1348	1318
1253	1336	1423	1483	1307	1499
1348	1219	1381	1470	1326	1331
1209	1269	1314	1104	1342	1353
1492	1604	1599	1132	1207	1316
1556	1682	1494	1621	1405	1248

18 FEB 1974

1227	1271	1416	1536	1646	1434
1216	1328	1557	1516	1342	1361
1329	1619	1493	1376	1259	1261
1654	1494	1449	1125	1194	1028
1500	1452	1368	1273	1375	1179
1548	1436	1175	1312	1332	1447

23 FEB 1974

1018	662	803	999	1202	1528
877	799	993	1093	1036	865
1023	1239	1127	1143	1280	684
1100	1104	1048	867	1015	1423
937	756	1180	1185	1241	1338
831	735	995	1122	1337	1382

26 FEB 1974

Fig. 31. Long wave radiational cooling rate from 100 mb to the surface, in 10^3 °C/day, at the grid points used for this study (Ref. Fig. 5).

384	390	366	370	413	446
382	436	442	426	436	366
442	432	411	424	460	393
438	431	367	307	475	493
437	427	348	366	315	512
393	441	295	517	511	507

18 FEB 1974

340	316	291	412	395	384
412	329	465	402	474	451
411	345	428	393	470	406
323	349	427	447	406	358
325	278	465	460	416	371
329	331	412	495	424	480

23 FEB 1974

365	267	292	384	339	482
310	364	369	244	258	302
370	427	383	453	169	313
451	381	224	234	308	455
403	360	418	203	269	398
386	294	319	344	275	523

26 FEB 1974

Fig. 32. Short wave radiational heating rate from 100 mb to the surface, in 10^3 °C/day, at the grid points used for this study (Ref. Fig. 5).

716	790	849	1020	935	872
871	900	981	1056	871	1133
905	787	970	1047	865	938
771	837	947	797	867	861
1054	1177	1251	765	891	804
1163	1240	1199	1105	894	741

18 FEB 1974

888	955	1125	1124	1250	1050
804	999	1092	1114	868	910
918	1274	1066	983	790	876
1332	1145	1023	678	788	670
1175	1175	903	813	959	808
1219	1105	763	817	908	967

23 FEB 1974

653	395	511	615	863	1046
567	435	625	849	778	563
653	812	744	690	1111	371
650	723	824	633	708	967
534	396	763	982	952	940
446	441	676	778	1061	859

26 FEB 1974

Fig. 33. Net radiational cooling rate from 100 mb to the surface, in 10^3 °C/day, at the grid points used for this study (Ref. Fig. 5).

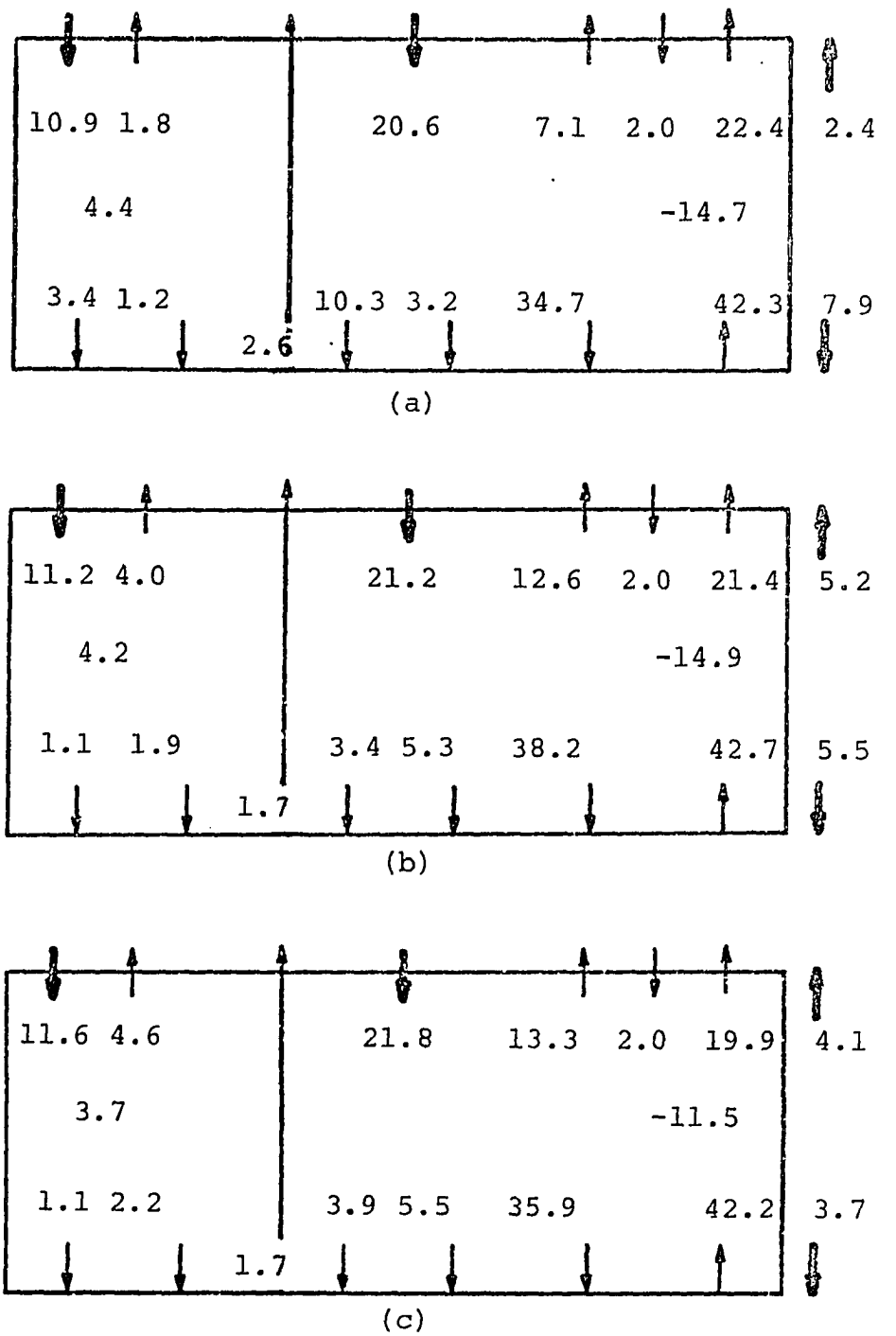

Fig. 34. Schematic representation of the average radiation budgets of the atmospheric column from 100 mb to the surface for (a) February 18, 1974; (b) February 23, 1974; and (c) February 26, 1974 in the AMTEX area. Terms are identified in Figure 4. Units are in mW cm^{-2}. The fluxes are positive in the direction of the arrows.

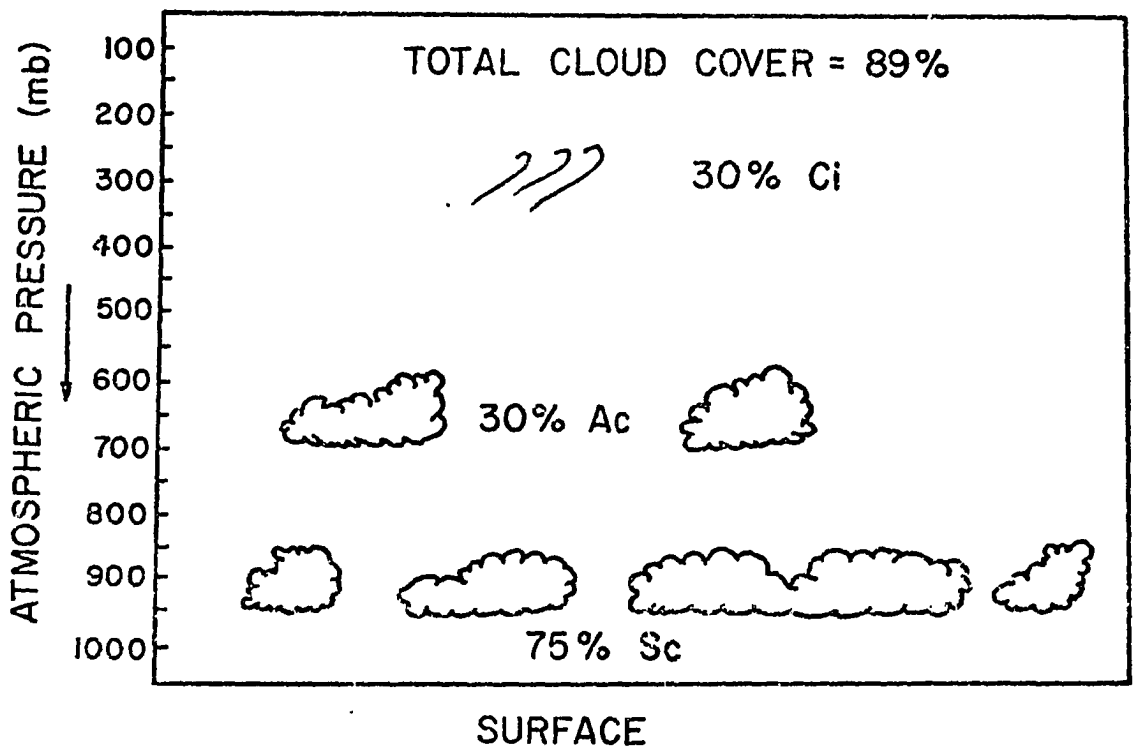

Fig. A-1. Example of the type of information available for the composite three layer cloud analysis derived from the 3DNEPH data. Depicted is the spacial estimate of clouds at a typical grid point in the AMTEX region on February 23, 1974, at 0900 JST. Cloud bases and tops are fitted to the nearest 50 mb constant pressure level.

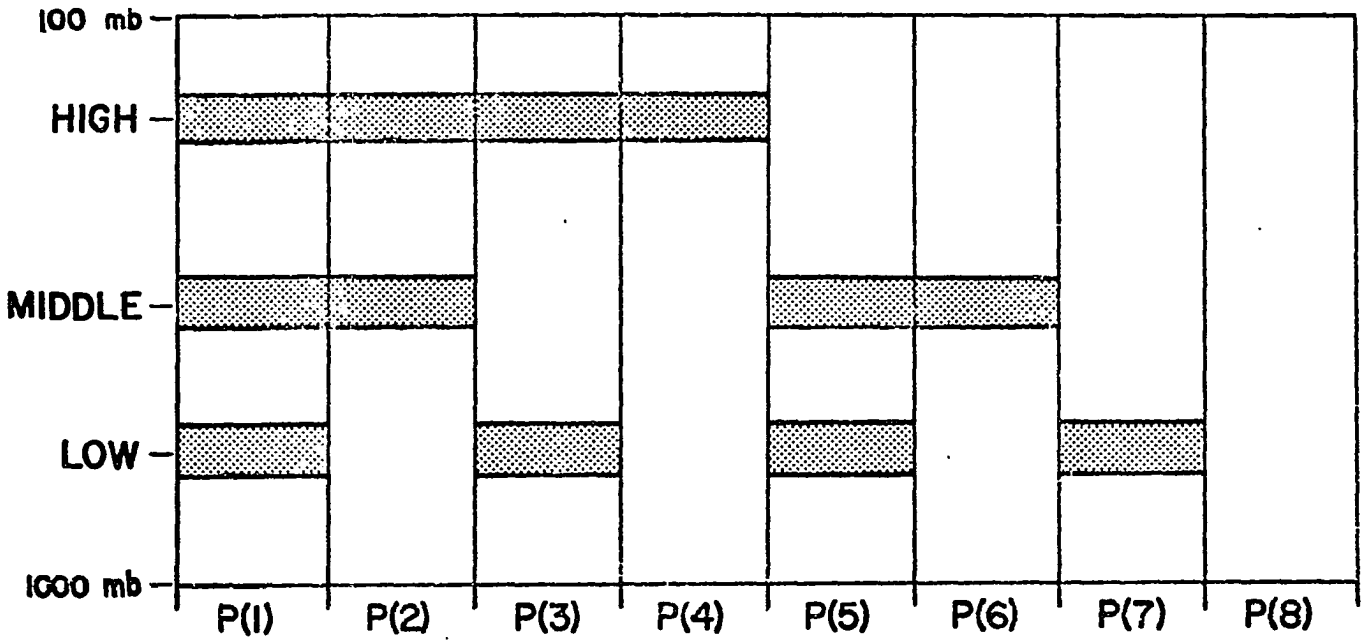

Figure A-2. Schematic diagram of the eight possible situations a stream of radiation could encounter with three cloud layers present. The P's refer to the probability of encounter (see text).